

# A near-IR study of the host galaxies of 2 Jy radio sources at $0.03 \lesssim z \lesssim 0.5$ – I. The data<sup>★</sup>

K. J. Inskip,<sup>1†</sup> C. N. Tadhunter,<sup>2</sup> R. Morganti,<sup>3,4</sup> J. Holt,<sup>5</sup> C. Ramos Almeida<sup>2,6</sup> and D. Dicken<sup>7</sup>

<sup>1</sup>Max-Planck-Institut für Astronomie, Königstuhl 17, D-69117 Heidelberg, Germany

<sup>2</sup>Department of Physics & Astronomy, University of Sheffield, Sheffield S3 7RH

<sup>3</sup>Netherlands Foundation for Research in Astronomy, Postbus 2, 7990 AA Dwingeloo, the Netherlands

<sup>4</sup>Kapteyn Astronomical Institute, University of Groningen, PO Box 800, 9700 AV Groningen, the Netherlands

<sup>5</sup>Leiden Observatory, Leiden University, Niels Bohrweg 2, NL-2333 CA Leiden, the Netherlands

<sup>6</sup>Instituto de Astrofísica de Canarias (IAC), C/Vía Láctea, s/n, E-38205, La Laguna, Tenerife, Spain

<sup>7</sup>Rochester Institute of Technology, 85 Lomb Memorial Drive, Rochester NY 14623, USA

Accepted 2010 May 11. Received 2010 May 11; in original form 2010 March 31

## ABSTRACT

We present the results of a program of  $K$ - and  $K_s$ -band imaging of a sample of 2 Jy radio galaxies with redshifts  $0.03 \lesssim z \lesssim 0.5$ , for which the host galaxy morphologies and structural parameters (effective radius, Sérsic index and unresolved nuclear point source contribution) have been determined using GALFIT. Two-thirds of our sample are best modelled as being hosted by massive elliptical galaxies with Sérsic indices of  $n = 4$ – $6$ , with the remainder being better suited either by a mixture of morphological components (usually a bulge plus a small, less luminous, disc component) or by more discy galaxy models with  $n = 1$ – $2$ . Our measured galaxy sizes are generally in very good agreement with other imaging programs, both space- and ground-based. We also determine a slightly higher average nuclear point source contribution than similar *Hubble Space Telescope* based programs. This is due to our inability to separate the active galactic nuclei emission from compact circum-nuclear stellar emission, but does not bias our modelling of the remainder of the host galaxies and our results remain robust. We also observe that roughly half of the objects in our sample are either undergoing major or minor merger activity or are clearly morphologically disturbed.

**Key words:** galaxies: active – galaxies: evolution – galaxies: interactions – galaxies: photometry – galaxies: structure – infrared: galaxies.

## 1 INTRODUCTION

Over the last decade, it has become increasingly apparent that not only do supermassive black holes reside in the centres of all massive galactic bulges, but also that their ongoing evolution is strongly coupled, despite nine orders of magnitude difference between the relevant spatial scales of the black hole and its galactic host (Kormendy 1993; Magorrian et al. 1998; Ferrarese & Merritt 2000; Gebhardt et al. 2000; Merritt & Ferrarese 2001; Cattaneo & Bernardi 2003; Marconi & Hunt 2003; Häring & Rix 2004). Regardless of the physical driving mechanisms for these correlations, it is certain that understanding the periods of active galactic nuclei (AGN) activity,

when the central black hole is most able to grow via accretion, is of crucial importance for building up a cogent theoretical framework for galaxy evolution in general (e.g. Yu & Tremaine 2002; Shankar et al. 2004; Marconi et al. 2004 and references therein). This problem poses two central, interlinked questions: what is the nature of an active galaxy, and how do they differ from the inactive population of galaxies from which they are (presumably) drawn?

Extragalactic radio sources play a particularly important role in such studies. Historically, they have been amongst the best studied distant AGN, due to the ease with which large samples of such objects could be assembled out to large redshifts. Under orientation-based unification schemes for radio galaxies and radio-loud quasars (e.g. Barthel 1989; Urry & Padovani 1995), they provided a perfect laboratory for studying the host galaxies of radio-loud AGN without the complicating presence of an unobscured bright quasar nucleus. Additionally, the presence of extensive powerful radio emission directly links the behaviour of these systems from the small scales of the central accreting black hole out to many hundreds or thousands

<sup>★</sup>Based on observations collected at the European Southern Observatory, Chile [programs 074.B-0296(A), 074.B-0296(B), 075.B-0674(A) and 078.B-0500(A)].

†E-mail: inskip@mpia-hd.mpg.de

of kiloparsec into the surrounding intergalactic medium (IGM). Early studies of the proto-typical 3CR sources suggested that the host galaxies of these radio sources were members of a remarkably uniform population, and seemed to be ‘standard candles’ to within  $\sim 0.3$  mag (Lilly & Longair 1984), with characteristic effective radii of up to 15 kpc and IR magnitudes dominated by emission from an old stellar population formed at  $z > 5$  (Best, Longair & Röttgering 1998). However, subsequent revisions to the most widely accepted cosmological model (e.g. Hinshaw et al. 2009) and an improved understanding of structure formation in the Universe (e.g. Springel et al. 2005) add considerable complexity to this picture.

While a radio source *may* undergo several active phases (e.g. Haehnelt & Rees 1993; Saikia & Jamrozy 2009 and references therein), this does not imply that any given radio source would necessarily have been active in the past, or will be so again in the future. This opens up the scenario whereby radio galaxies at different epochs could be drawn from quite different galaxy populations: might this indeed be the case? The tightness of the  $K-z$  relation (e.g. Inskip et al. 2002; Willott et al. 2003; Rocca-Volmerange et al. 2004) and the total near-IR luminosities of their host galaxies (Seymour et al. 2007) suggest that radio sources are hosted by a relatively homogeneous, high-mass (up to  $\sim 10^{12} M_{\odot}$ ) population of galaxies over a wide redshift range. Even at higher redshifts, while morphological studies have shown that some sources are still undergoing active assembly, radio source host galaxies at redshifts of  $z \sim 2-3$  are in general similar in size to those nearby (e.g. van Breugel et al. 1998; Pentericci et al. 2001). However, the increased luminosity of high-redshift radio galaxies relative to passive evolution models goes against the simplest picture of closed-box evolution of a single population of galaxies.

The high mass of radio source host galaxies at all epochs provides an additional constraint. Since  $z \sim 1$ , the most massive members of the elliptical galaxy population have shown little evolution in mass (e.g. Heavens et al. 2004; Thomas et al. 2005). Although subsequent episodes of AGN activity in massive galaxies could be triggered by minor mergers or galaxy interactions which lead to little additional change in galaxy mass, the links between periods of black hole accretion and galaxy growth (as evidenced by the black hole mass versus bulge mass relation) limits the ability of such objects to repeatedly host powerful, high accretion-rate AGN in more recent cosmic epochs. On top of this, it has been theorized that the very presence of a powerful radio source and/or AGN can limit the potential for further galaxy growth, via heating of the local environment (e.g. Fabian et al. 2000; McNamara & Nulsen 2007; Croton & Farrar 2008; De Young 2010). Equally, the actively accreting lower redshift systems have likely been assembled from their less-massive constituent progenitor objects too recently to have hosted powerful AGN at high redshifts.

Similarly, at different redshifts the powerful radio source population samples different environments (e.g. Lilly & Prestage 1987; Yates, Miller & Peacock 1989; Hill & Lilly 1991; Best 2000), with a tendency towards more highly clustered objects at higher redshifts. It is now clear that galaxies are subject to so-called ‘cosmic downsizing’, by which both star formation (e.g. Cowie et al. 1996; Juneau et al. 2005) and AGN activity (e.g. Granato et al. 2004; De Lucia et al. 2006; Croton et al. 2006; Merloni & Heinz 2008; Martini, Sivakoff & Mulchaey 2009; Shen 2009) become increasingly more prevalent in lower mass objects at later cosmic epochs, and in less dense environments.

The inherent changes in the host galaxy population highlight the essential need to effectively characterize their properties at all redshifts. Without a clear handle on what a radio galaxy *is* at any given

epoch, it is practically impossible to determine how it may or may not differ from the underlying inactive galaxy population, or from the population of radio-quiet AGN. What are the characteristic sizes of powerful radio galaxies, and how does this parameter vary with redshift and/or radio power? Is the scatter in the  $K-z$  relation solely due to variations in galaxy mass, or can it be accounted for at least in part by variations in the host galaxy stellar populations? Do the host galaxies show signs of recent merger activity, and how does the proportion of merging/disturbed sources compare with that of normal galaxies? Is there any dependence of galaxy morphology on local environment, or on the radio source/AGN properties? With such physical characteristics of the host galaxies pinned down, deeper questions may then be posed on the nature of *how* AGN and radio source activity are triggered, e.g.: whether triggering occurs due to major or minor interactions or the more gradual infall of material; the prevalence of different triggering modes; the details of the timeline of events involved and any timelags between star formation and AGN/radio source activity; and the links between such processes and the evolution and observed morphological characteristics of the host galaxies.

In order to investigate these issues, we turn not to the 3CR sample, but instead to the similarly well-studied 2Jy sample of southern radio sources at  $z < 0.5$  (Tadhunter et al. 1993; Morganti, Killeen & Tadhunter 1993). This sample is unique in the sense that it is the *only* major sample of powerful radio galaxies for which complete, high-quality optical continuum and emission line spectra, as well as radio imaging data, exist for all the objects, alongside near- and mid-IR imaging and spectroscopy for most sources. One particular advantage of this sample is that the combination of the mid-IR data and optical spectra allows us to separately determine the extent of both obscured and unobscured star formation activity within the host galaxies, as well as providing two independent measures of the degree of nuclear activity (via the  $24 \mu\text{m}$  emission and the optical line emission). Our current data set consists of ground-based near-IR imaging of the majority of the sample objects. These data will be used to obtain accurate photometric magnitudes, and to thoroughly characterize the host galaxy structural properties as observed in this wavelength regime (galaxy profile, effective radius and the extent of any nuclear point source contamination from the AGN), and how they compare to other radio galaxy samples. We will also make a preliminary assessment of the prevalence of visible merger activity within the sample (either ongoing or having occurred in the recent past); this issue is expanded on in our analysis of optical imaging data for the 2Jy sample (Ramos Almeida et al., submitted hereafter RA10).

Having characterized the morphological properties of the host galaxies, in Paper II of this series we will extend our investigation to the more global properties of the sample. By combining galaxy morphologies with our data on the host galaxy stellar populations, the results of the current paper will be used to investigate the nature of the scatter in the  $K-z$  relation, and how well it can be accounted for in terms of galaxy mass and recent star formation activity. We will also use literature data for other radio galaxy surveys at higher redshift to examine how redshift and radio power impact on the observed trends. Finally, together with the results of RA10, we will assess in Paper II how closely morphological signatures of merger activity correlate with the degree of recent star formation, the host galaxy morphologies and the size/age of the radio source, helping us to build a clearer picture of the variety of different physical modes of AGN triggering in these sources. Further to this work, these data will also be used in conjunction with the existing optical data (RA10) to also constrain the local environments of the host galaxies

(Ramos Almeida et al., in preparation), and to comprehensively assess the impact of environment on the properties of powerful radio sources and their host galaxies.

In Section 2, we provide details of our observed sample. Our observations and data reduction processes are described in Section 3. In Section 4, we present our observational results and our 2D modelling of the host galaxies, while our discussion and conclusions are presented in Sections 5 and 6, respectively. A more extensive analysis of this data set is postponed to a second paper in this series.

Throughout this paper, we assume cosmological parameters of  $\Omega_0 = 0.27$ ,  $\Omega_\Lambda = 0.73$  and  $H_0 = 71 \text{ km s}^{-1} \text{ Mpc}^{-1}$ .

## 2 SAMPLE DETAILS

The sample of galaxies studied in this paper has been selected from the 2Jy sample of Wall & Peacock (1985) which has flux densities  $S_{2.7\text{GHz}} > 2 \text{ Jy}$  and declinations  $\delta < 10^\circ$ , with the addition of PKS 0347+05 which was later found to meet the same criteria (di Serego-Alighieri et al. 1994). Optical classifications have been determined for these objects on the basis of previous optical spectroscopic observations (Tadhunter et al. 1998) and their optical appearance (Wall & Peacock 1985). Sources with  $[\text{O III}]\lambda 5007$  emission line equivalent widths  $< 10 \text{ \AA}$  are classified as weak line radio galaxies (WLRGs). The remainder are classified as narrow line radio galaxies (NLRGs), broad line radio galaxies (BLRGs) and quasars. The quasars were classified by Wall & Peacock (1985) on the basis of their stellar appearance on optical images, while the NLRGs and BLRGs are classified according to whether or not their optical spectra show evidence for broad line emission. Our sample excludes sources optically classified as quasars, and was primarily selected within the redshift range  $0.05 < z < 0.5$  and with right ascensions of  $19^{\text{h}}00 < RA < 14^{\text{h}}00$ . Due to the availability of observing time on different instruments, this was later extended to redshifts of  $0.03 < z < 0.5$  within the right ascension range of  $21^{\text{h}}00 < RA < 14^{\text{h}}00$ , and  $0.05 < z < 0.5$  within the ranges  $14^{\text{h}}00 < RA < 16^{\text{h}}00$  and  $17^{\text{h}}30 < RA < 21^{\text{h}}00$ . Of the resulting sample of 46 sources, we have obtained observations of 43. PKS 0620–52 was dropped from the sample due to its proximity to the bright star Canopus, while PKS 1839–48 was lost due to observing time constraints. PKS 1954–55 is known to have a bright foreground star in close proximity to its nucleus, and

was also excluded. Despite not reaching 100 per cent completeness, this sample is a representative, unbiased 93 per cent complete subset of the whole.

## 3 OBSERVATIONS AND DATA REDUCTION

### 3.1 UKIRT K-band imaging

The United Kingdom Infra-Red Telescope (UKIRT) observations were carried out on 2004 September 13, 2004 September 14 and 2004 September 15 using UFTI (the UKIRT Fast-Track Imager; Roche et al. 2003). UFTI is a 1–2.5  $\mu\text{m}$  camera with a  $1024 \times 1024$  HgCdTe array and a plate scale of 0.091 arcsec per pixel, which gives a field of view of 92 arcsec. Details of the observing conditions are provided in Table 1, with further details of the sources observed and the individual exposure times listed in Table 2.

All observations used a nine-point jitter pattern, with offsets of roughly 10 arcsec between each 1 min exposure. The observational data were dark subtracted, and masked for bad pixels. The data for each source (or several consecutive sources for the lower redshift objects for which only a handful of individual exposures were obtained) were combined and median filtered to create a first-pass sky flat-field image, which accounted for the majority of the pixel-to-pixel variations of the chip. However, large-scale illumination gradients remained, due to the changing position of the telescope over the night. To correct for this, smaller groups of nine to 18 first pass flat-fielded images were similarly combined to create residual sky flat-field images. Applying these residual flat-fields to the first-pass flat-fielded data successfully accounted for this effect. Bright objects on the fully flat-fielded images were then masked out, and the whole process repeated, allowing the data to be cleanly flat-fielded without any contamination from stars or galaxies. The flat-fielded data for each source were sky-subtracted and combined using the IRAF package DIMSUM, creating a final mosaicked image of approximately  $115 \times 115 \text{ arcsec}^2$ , with the highest signal-to-noise ratio level restricted to the central  $70 \times 70 \text{ arcsec}^2$ . The data were flux calibrated using observations of standard stars selected from the UKIRT faint standards catalogue.

Photometry was carried using the IRAF package APPHOT and a single sky annulus; 4 arcsec, 5 arcsec and 9 arcsec diameter

**Table 1.** Details of the observational data used in this paper. Seeing measurements are given for the wavelength of the observations. Observations were photometric except where noted otherwise.

Date	Instrument	Filter	Plate scale (arcsec pixel <sup>-1</sup> )	Typical field of view (arcmin <sup>2</sup> )	Seeing (arcsec)	Notes
20040913	UFTI	<i>K</i>	0.0909	$1.5 \times 1.5$	0.4–0.5	
20040914	UFTI	<i>K</i>	0.0909	$1.5 \times 1.5$	0.5–1.0	
20040915	UFTI	<i>K</i>	0.0909	$1.5 \times 1.5$	0.5–0.6	
20041114	SOFI – large field	<i>K<sub>S</sub></i>	0.288	$5.0 \times 5.0\text{--}8.0 \times 8.0$	0.9–1.35	1
20041115	SOFI – large field	<i>K<sub>S</sub></i>	0.288	$5.0 \times 5.0\text{--}8.0 \times 8.0$	0.6–0.95	2
20050226	SOFI – small field	<i>K<sub>S</sub></i>	0.144	$3.0 \times 3.0$	0.55–1.1	3
20050228	SOFI – small field	<i>K<sub>S</sub></i>	0.144	$3.0 \times 3.0$	0.55–1.2	
20050301	SOFI – small field	<i>K<sub>S</sub></i>	0.144	$3.0 \times 3.0$	0.65–1.1	
20050315	SOFI – small field	<i>K<sub>S</sub></i>	0.144	$3.0 \times 3.0$	0.65–1.4	
20050712	ISAAC	<i>K<sub>S</sub></i>	0.072	$1.5 \times 1.5\text{--}2.0 \times 2.0$	0.6–2.5	
20050713	ISAAC	<i>K<sub>S</sub></i>	0.072	$1.5 \times 1.5\text{--}2.0 \times 2.0$	0.6–1.5	4
20061113	SOFI – small field	<i>K<sub>S</sub></i>	0.144	$3.0 \times 3.0$	0.6–0.9	

*Notes.* [1] Initially photometric; observations later abandoned due to cloud.

[2] Patchy thin cirrus at times, and partially photometric.

[3] Non-photometric ( $\sim 0.1\text{--}0.6$  mag extinction).

[4] Observations cut short due to cloud.

**Table 2.** Sample details. Columns 2, 3 and 4 list any alternative name, the optical classification and redshift of each of the sources in our sample. The instrument used, observation date and exposure time in minutes for our infrared observations are listed in Columns 5, 6 and 7, respectively. Column 8 lists the PSF FWHM for the observations of each source in arcsec.

Source [1]	Alt. name [2]	Optical classification [3]	$z$ [4]	Instrument [5]	Date [6]	Exposure [7]	PSF FWHM [8]
PKS 0023–26		NLRG	0.32	SOFI	20041115	94	0.91
PKS 0034–01	3C15	WLRG	0.07	SOFI	20041115	20	0.86
PKS 0035–02	3C17	BLRG	0.22	UFTI	20040913, 20040914	36, 18	0.54
PKS 0038+09	3C18	BLRG	0.19	UFTI	20040915	45	0.52
PKS 0039–44		NLRG	0.346	SOFI archive	20050815	1	–
PKS 0043–42		WLRG	0.12	SOFI	20041115	25	0.93
PKS 0055–01	3C29	WLRG	0.05	SOFI	20041115	5	0.89
PKS 0105–16	3C32	NLRG	0.40	SOFI	20061113	75	0.86
PKS 0131–36	NGC 0612	WLRG	0.03	SOFI	20041114	20	1.15
PKS 0213–132	3C62	NLRG	0.15	SOFI	20041115	30	0.95
PKS 0305+03	3C78	WLRG	0.03	SOFI	20041114	4	1.35
PKS 0325+02	3C88	WLRG	0.03	SOFI	20041114	5	1.24
PKS 0347+05	4C+05.16	WLRG	0.34	UFTI	20040913, 20040914	36, 18	0.45
PKS 0349–27		NLRG	0.07	SOFI	20041115	30	0.84
PKS 0404+03	3C105	NLRG	0.09	SOFI	20050226, 20050228	95, 95	0.73
PKS 0427–53	IC2082	WLRG	0.04	SOFI	20041115	5	0.88
PKS 0430+05	3C120	BLRG	0.03	SOFI	20061113	10	0.76
PKS 0442–28		NLRG	0.15	SOFI	20041115	30	0.86
PKS 0453–20	NGC 1692	WLRG	0.04	SOFI	20041115	5	0.79
PKS 0518–45	Pictor A	BLRG	0.04	SOFI	20041115	25	0.85
PKS 0521–36	ESO 362–G021	BLRG	0.06	SOFI	20041115	20	0.82
PKS 0625–53	ESO 161–IG007	WLRG	0.05	SOFI	20041115	5	0.79
PKS 0625–35		WLRG	0.06	SOFI	20041115, 20061113	20, 20	0.59
PKS 0806–10	3C195	NLRG	0.11	SOFI	20041115, 20061113	20, 20	0.66
PKS 0859–25		NLRG	0.31	SOFI	20050228	20	0.55
PKS 0915–11	Hydra A	WLRG	0.05	SOFI, SOFI archive	20041115, 20031213	10, 38	0.86
PKS 0945+07	3C227	BLRG	0.09	SOFI	20050228	22	0.68
PKS 1306–09		NLRG	0.46	SOFI	20050301	95	0.66
PKS 1547–79		BLRG	0.48	SOFI	20050315	95	0.67
PKS 1549–79		BLRG?	0.15	ISAAC	20050712	27	0.78
PKS 1559+02	3C327	NLRG	0.11	ISAAC	20050713	9	0.66
PKS 1733–56		BLRG	0.10	ISAAC	20050714	20	1.05
PKS 1814–63		NLRG	0.06	ISAAC	20050712	18	0.93
PKS 1932–46		BLRG	0.23	SOFI	20061113	50	0.78
PKS 1934–63		NLRG	0.18	SOFI	20061113	45	0.89
PKS 1949+02	3C403	NLRG	0.06	ISAAC	20050712	36	0.93
PKS 2104–25	NGC 7018		0.039	SOFI archive	19990414	60	–
PKS 2153–69	ESO 075–G041	BLRG	0.03	ISAAC	20050712	9	0.76
PKS 2211–17	3C444	WLRG	0.15	ISAAC	20050712	18	0.86
PKS 2221–02	3C445	BLRG	0.06	SOFI	20061113	5	0.77
PKS 2250–41		NLRG	0.31	SOFI	20061113	50	0.67
PKS 2313+03	3C459	NLRG	0.22	UFTI, UFTI, SOFI	20040914, 20040915, 20061113	27, 27, 45	0.53
PKS 2356–61		NLRG	0.10	ISAAC	20050712	27	0.68

circular apertures were used, and also a 64 kpc diameter circular aperture in the rest frame of the source (for consistency with earlier  $K$ -band studies of radio galaxy hosts; Eales et al. 1997; Jarvis et al. 2001; Inskip et al. 2002; Willott et al. 2003). These data are presented in Table 3. We also include the 64 kpc aperture magnitudes for each source after the modelling and removal of any bright contaminating objects within the aperture, with the exception of any object which appears to be physically interacting with the target galaxy. The error on our zero-point measurements is combined in quadrature with the standard APPHOT uncertainties: the percentage error due to the Poisson noise from the detected counts, the percentage random error due to the sky counts in the aperture and the percentage systematic error due to the accuracy to which the mean sky value can be calculated. The resulting mag-

nitudes have been corrected for Galactic extinction using the  $E(B - V)$  for the Milky Way from the NASA Extragalactic Data base (NED) and the parametrized Galactic extinction law of Howarth (1983).

### 3.2 SOFI $K_S$ -band imaging

$K_S$ -band observations were obtained on the nights of 2004 November 14, 2004 November 15, 2005 February 26, 2005 February 28, 2005 March 1, 2005 March 15 and 2006 November 13, using the Son of ISAAC (SOFI; Moorwood, Cuby & Lidman 1998a) instrument on the European Southern Observatory (ESO) 3.5-m New Technology Telescope (NTT), as part of the ESO observing programmes 074.B-0296(A), 074.B-0296(B) and 078.B-0500(A). On

**Table 3.** Results of our infrared observations. In Columns 2–6, we present the results of aperture photometry carried out within four different aperture sizes: 4, 5 and 9 arcsec diameter aperture  $K$  or  $K_S$  magnitudes are given in Columns 2, 3 and 4, respectively, along with the associated errors. Column 5 lists the aperture magnitudes and errors obtained using a fixed metric aperture 64 kpc in diameter in the rest frame of each source. In Column 6, we present the same aperture magnitude after removal of the flux from any contaminating object (see text for full details). Column 7 presents the same data after K-correcting the  $K_S$ -band observations to the  $K$ -band filter. All magnitudes have been corrected for galactic extinction using  $E(B - V)$  values taken from the NED and the parametrized galactic extinction law of Howarth (1983).

Source	Magnitudes in different apertures					
[1]	4 arcsec [2]	5 arcsec [3]	9 arcsec [4]	64 kpc [5]	64 kpc (clean) [6]	64 kpc (K-corrected) [7]
PKS 0023–26	15.632 ± 0.057	15.501 ± 0.055	15.176 ± 0.051	14.651 ± 0.045	15.036 ± 0.054	15.017 ± 0.056
PKS 0034–01	13.571 ± 0.036	13.403 ± 0.035	13.050 ± 0.034	12.569 ± 0.037	12.569 ± 0.037	12.571 ± 0.037
PKS 0035–02	14.459 ± 0.056	14.384 ± 0.056	14.205 ± 0.055	14.100 ± 0.055	14.104 ± 0.055	14.104 ± 0.055
PKS 0038+09	14.402 ± 0.035	14.368 ± 0.034	14.305 ± 0.033	14.216 ± 0.036	14.296 ± 0.037	14.296 ± 0.037
PKS 0039–44	15.771 ± 0.053	15.644 ± 0.057	15.537 ± 0.086	15.411 ± 0.122	15.411 ± 0.122	15.388 ± 0.122
PKS 0043–42	13.853 ± 0.037	13.703 ± 0.036	13.369 ± 0.034	12.977 ± 0.036	12.999 ± 0.036	12.988 ± 0.036
PKS 0055–01	13.560 ± 0.262	13.237 ± 0.259	12.496 ± 0.255	11.554 ± 0.300	11.596 ± 0.282	11.599 ± 0.282
PKS 0105–16	15.801 ± 0.055	15.686 ± 0.052	15.475 ± 0.048	15.419 ± 0.049	15.419 ± 0.049	15.380 ± 0.049
PKS 0131–36	11.760 ± 0.031	11.465 ± 0.031	10.783 ± 0.030	9.553 ± 0.030	9.563 ± 0.030	9.566 ± 0.030
PKS 0213–132	14.515 ± 0.365	14.385 ± 0.364	14.029 ± 0.364	13.502 ± 0.366	13.502 ± 0.366	13.492 ± 0.366
PKS 0305+03	11.491 ± 0.031	11.207 ± 0.031	10.576 ± 0.030	9.155 ± 0.030	9.156 ± 0.031	9.159 ± 0.031
PKS 0325+02	12.938 ± 0.033	12.659 ± 0.033	12.027 ± 0.032	10.366 ± 0.034	10.388 ± 0.034	10.391 ± 0.034
PKS 0347+05	14.685 ± 0.058	14.576 ± 0.057	14.308 ± 0.056	13.963 ± 0.054	14.283 ± 0.056	14.283 ± 0.056
PKS 0349–27	13.882 ± 0.037	13.750 ± 0.037	13.433 ± 0.035	12.675 ± 0.034	12.853 ± 0.037	12.855 ± 0.037
PKS 0404+03	14.131 ± 0.051	14.000 ± 0.051	13.713 ± 0.050	13.343 ± 0.050	13.417 ± 0.055	13.411 ± 0.055
PKS 0427–53	12.320 ± 0.032	12.086 ± 0.032	11.536 ± 0.031	9.984 ± 0.031	10.067 ± 0.031	10.071 ± 0.031
PKS 0430+05	10.778 ± 0.011	10.727 ± 0.011	10.587 ± 0.011	10.018 ± 0.100	10.018 ± 0.100	10.021 ± 0.100
PKS 0442–28	13.742 ± 0.036	13.644 ± 0.036	13.410 ± 0.035	13.134 ± 0.034	13.160 ± 0.035	13.150 ± 0.035
PKS 0453–20	12.578 ± 0.032	12.312 ± 0.032	11.698 ± 0.031	10.218 ± 0.032	10.252 ± 0.032	10.256 ± 0.032
PKS 0518–45	12.542 ± 0.032	12.483 ± 0.032	12.316 ± 0.032	11.820 ± 0.034	12.015 ± 0.037	12.019 ± 0.037
PKS 0521–36	11.342 ± 0.031	11.283 ± 0.031	11.151 ± 0.031	10.901 ± 0.031	10.913 ± 0.031	10.916 ± 0.031
PKS 0625–53	12.537 ± 0.192	12.269 ± 0.192	11.641 ± 0.191	10.022 ± 0.191	10.042 ± 0.191	10.045 ± 0.191
PKS 0625–35	12.052 ± 0.014	11.889 ± 0.013	11.506 ± 0.012	9.817 ± 0.011	10.724 ± 0.047	10.727 ± 0.047
PKS 0806–10	12.820 ± 0.017	12.719 ± 0.016	12.467 ± 0.016	12.137 ± 0.016	12.137 ± 0.016	12.126 ± 0.016
PKS 0859–25	15.185 ± 0.060	15.048 ± 0.058	14.732 ± 0.055	14.370 ± 0.054	14.758 ± 0.069	14.742 ± 0.069
PKS 0915–11	13.246 ± 0.108	12.946 ± 0.108	12.269 ± 0.108	10.817 ± 0.108	10.868 ± 0.108	10.871 ± 0.108
PKS 0945+07	12.678 ± 0.047	12.635 ± 0.047	12.535 ± 0.046	12.367 ± 0.047	12.376 ± 0.048	12.370 ± 0.048
PKS 1306–09	15.300 ± 0.051	15.234 ± 0.050	14.906 ± 0.046	14.757 ± 0.045	15.120 ± 0.062	15.080 ± 0.062
PKS 1547–79	15.296 ± 0.044	15.259 ± 0.044	15.090 ± 0.044	15.030 ± 0.044	15.185 ± 0.044	15.142 ± 0.044
PKS 1549–79	12.466 ± 0.043	12.429 ± 0.043	12.362 ± 0.043	12.280 ± 0.043	12.319 ± 0.043	12.309 ± 0.043
PKS 1559+02	13.388 ± 0.044	13.189 ± 0.044	12.777 ± 0.043	12.205 ± 0.044	12.205 ± 0.044	12.194 ± 0.044
PKS 1733–56	13.396 ± 0.044	13.222 ± 0.044	12.892 ± 0.043	12.058 ± 0.043	12.485 ± 0.043	12.474 ± 0.043
PKS 1814–63	12.775 ± 0.043	12.596 ± 0.043	12.317 ± 0.043	11.851 ± 0.043	11.896 ± 0.043	11.899 ± 0.043
PKS 1932–46	15.413 ± 0.046	15.301 ± 0.044	15.083 ± 0.040	14.971 ± 0.044	14.971 ± 0.044	14.962 ± 0.044
PKS 1934–63	14.845 ± 0.036	14.665 ± 0.034	14.220 ± 0.028	13.931 ± 0.026	14.023 ± 0.030	14.016 ± 0.030
PKS 1949+02	12.662 ± 0.043	12.453 ± 0.043	12.001 ± 0.043	10.121 ± 0.043	11.333 ± 0.043	11.336 ± 0.043
PKS 2153–69	11.998 ± 0.043	11.808 ± 0.043	11.362 ± 0.043	10.036 ± 0.043	10.180 ± 0.044	10.183 ± 0.044
PKS 2211–17	14.975 ± 0.046	14.671 ± 0.045	14.008 ± 0.044	13.111 ± 0.044	13.422 ± 0.048	13.412 ± 0.048
PKS 2221–02	11.602 ± 0.013	11.569 ± 0.013	11.503 ± 0.013	11.448 ± 0.013	11.448 ± 0.013	11.451 ± 0.013
PKS 2250–41	15.813 ± 0.055	15.739 ± 0.053	15.573 ± 0.051	15.508 ± 0.057	15.508 ± 0.057	15.492 ± 0.057
PKS 2313+03 ( $K$ )	13.961 ± 0.043	13.890 ± 0.042	13.752 ± 0.042	13.639 ± 0.042	13.639 ± 0.042	13.639 ± 0.042
PKS 2313+03 ( $K_S$ )	14.005 ± 0.026	13.932 ± 0.025	13.795 ± 0.024	13.672 ± 0.024	13.672 ± 0.024	13.664 ± 0.024
PKS 2356–61	13.704 ± 0.044	13.515 ± 0.044	13.115 ± 0.044	12.559 ± 0.044	12.559 ± 0.044	12.548 ± 0.044

most nights the instrument was used in the small field mode, which results in a plate scale of 0.144 arcsec per pixel. The large field mode, with a plate scale of 0.288 arcsec per pixel, was used for the observations obtained on 20041115. Details of the observing conditions are provided in Table 1, with further details of the sources observed and the individual exposure times listed in Table 2. Generally, the observations of each source consisted of a number of 1 min exposures, with each observation subject to a random offset within a 40 arcsec diameter box. For the lower redshift objects in our sample (typically those with  $z < 0.1$ ) we switched to five 1 min integrations at fixed offsets.

The data were corrected for SOFI's interquadrant row cross-talk effect using an adapted version of the SOFI crosstalk.cl IRAF script. Flat-fielding of the data was carried out using the following process: all target frames were combined, median filtered and normalized to a mean pixel value of 1.0 to create a first-pass flat-field image, which was then applied to each frame. Bright objects on the flat-fielded images were then masked out, and the process repeated with the masked frames, allowing the data to be cleanly flat-fielded without any contamination from stars or galaxies. The subsequent data reduction uses well-established techniques: the flat-fielded data were sky-subtracted and combined using the IRAF package DIMSUM.

Flux calibration used observations of the Near Infrared Camera and Multi-Object Spectrometer (NICMOS) Photometric Standard stars (Persson et al. 1998). Aperture photometry, galactic extinction corrections and uncertainties for the resulting magnitudes were determined in the same way as for the UFTI observations.

The observations carried out on the nights of 2004 November 15 and 2005 February 26 were unfortunately subject to the presence of variable patchy cirrus at the start and the end of the night. Regular observations of standard stars and good knowledge of the instrumental zero-point based on the previous night's observations allowed us to keep track of which sources were observed in partially non-photometric conditions, and the changing extent of the extinction due to thin clouds.

As an example, the bulk of our observations of PKS 0023–26 were obtained in non-photometric conditions. (Note that the use of repeated standard star observations confirmed that some of the observations made of this object were obtained in clear transparency conditions.) This presents several challenges. First, due to the strongly varying sky background level, the data are no longer best reduced in time-sequence order, such that sky subtraction is carried out for each frame based on the mean sky level of the frames immediately preceding and following the observation. Instead, the data are re-stacked in order of background sky brightness, and sky subtraction is carried out based on the mean sky background of the frames closest in sky luminosity. This procedure results in a high-quality final data product indistinguishable from one obtained in better observing conditions, which would not be the case for the more standard mode of sky subtraction. Secondly, while the non-photometric data are still useful for morphological studies, simple combination of frames with equal weighting does not result in the best signal-to-noise ratio level for the final image. We therefore monitor the flux of bright objects and the background noise level in each frame, and our final image is produced from a weighted combination of individual frames according to the signal-to-noise ratio level applicable for each. Monitoring the flux level of bright objects in each frame is also of great importance for selecting any frames which may be free of extinction due to cirrus, particularly for the stars with Two-Micron All-Sky Survey (2MASS) magnitudes available within the instrumental field of view. In the case of PKS 0023–26, the final five frames obtained were identified as being free of extinction, and combined together to make a 'photometric-equivalent' final product separate from that used for our analysis of the galaxy morphologies. For PKS 0213–132, even the best frames were not obtained in clear transparency conditions, but from the examination of 2MASS object fluxes we have confirmed the extinction level at 1.2 mag for these frames, and applied the appropriate correction to the derived magnitudes.

For the data obtained on the night of 2004 November 15, the bulk of the sources were observed under clear-transparency conditions. For most of the remainder, either reliable photometric-equivalent images were produced, or further data were obtained. Photometric observations of PKS 0404+03 were obtained on 2005 February 28, while photometric observations of PKS 0806–10 and PKS 0625–35 were obtained on 2006 November 13. For the two outstanding sources observed only under non-photometric conditions, standard star fluxes and the variation of 2MASS object fluxes within the observational fields of view confirm that the observations of PKS 0055–01 and PKS 0043–42 were subject to a stable extinction of 0.9 and 0.2 mag, respectively. This, along with an associated estimate of the error on the extinction due to thin cirrus, has been accounted for in our photometry of these sources.

### 3.3 ISAAC $K_S$ -band imaging

Infrared  $K_S$ -band imaging observations of nine sources in our sample were carried out on 2005 July 12 and 2005 July 13 using the Infrared Spectrometer And Array Camera (ISAAC) (Moorwood et al. 1998b) as part of the ESO observing programme 075.B-0674(A). ISAAC is mounted on the Nasmyth B focus of the UT1 Antu unit of the Very Large Telescope (VLT). The plate scale for our observations is 0.148 arcsec per pixel. Details of the observing conditions are provided in Table 1, with further details of the sources observed and the individual exposure times listed in Table 2. We used a nine-point jitter pattern for these observations, and the data were reduced and flux-calibrated using the same process as for our SOFI observations. Aperture photometry, galactic extinction corrections and uncertainties for the resulting magnitudes were determined in the same way as for our other observations.

### 3.4 Archival data

Limited observations of three sources were obtained from the ESO archive.

For PKS 0039–44, four photometric 10 s spectroscopic acquisition observations [from program 075.B-0777(A)] taken on the night of 2005 August 18 using the SOFI instrument on the NTT are available. While the total exposure time is too brief for the observations to be of use for morphological studies, they are still useful for determining a galaxy magnitude.

Although we observed PKS 0915–11 on the night of 15 November 2004, none of our data for this source is photometric. We have obtained additional archival observations of this source (from program 072.A-0549(A)), consisting of 38  $10 \times 6$  s photometric exposures using the SOFI instrument in the large field mode on the NTT on the night of 2003 December 13.

PKS 2104–25 had been previously observed on the night of 1999 April 14 using the SOFI instrument in the large field mode on the NTT. These archive observations [from program 63.O-0448(A), studying the cluster Abell 3744 of which PKS 2104–25 is a member] consist of 36  $20 \times 5$  s photometric exposures. However, due to the relatively small size of the random offsets used in the observational sequence for PKS 2104–25 relative to the size of the galaxies in the cluster observed, the outer regions of the radio source host galaxy are unavoidably oversubtracted as part of the data reduction process, and these data are not useable for our purposes.

### 3.5 Photometric transformations

Our observations make use of two different filters: the Mauna Kea broad-band  $K$ -band filter in use with UFTI on UKIRT, and the shorter  $K_S$ -band filter in use with SOFI on the NTT and ISAAC on the VLT. Broadly speaking, at low redshifts the numerical difference in magnitudes obtained in either filter is negligible, due to the comparable shapes of the spectral energy distributions (SEDs) of both galaxies and the zero-magnitude A0V reference star Vega. However, for observations of higher redshift galaxies the situation becomes marginally more complex. Due to the flattening of the galaxy SED as redshift increases, the redder emission which would be included in the full  $K$ -band filter but not in the shorter  $K_S$ -band filter increases in strength relative to the emission included in both filters. Thus, the magnitude of a higher redshift galaxy observed in the  $K_S$  band is numerically larger than the value obtained in the  $K$

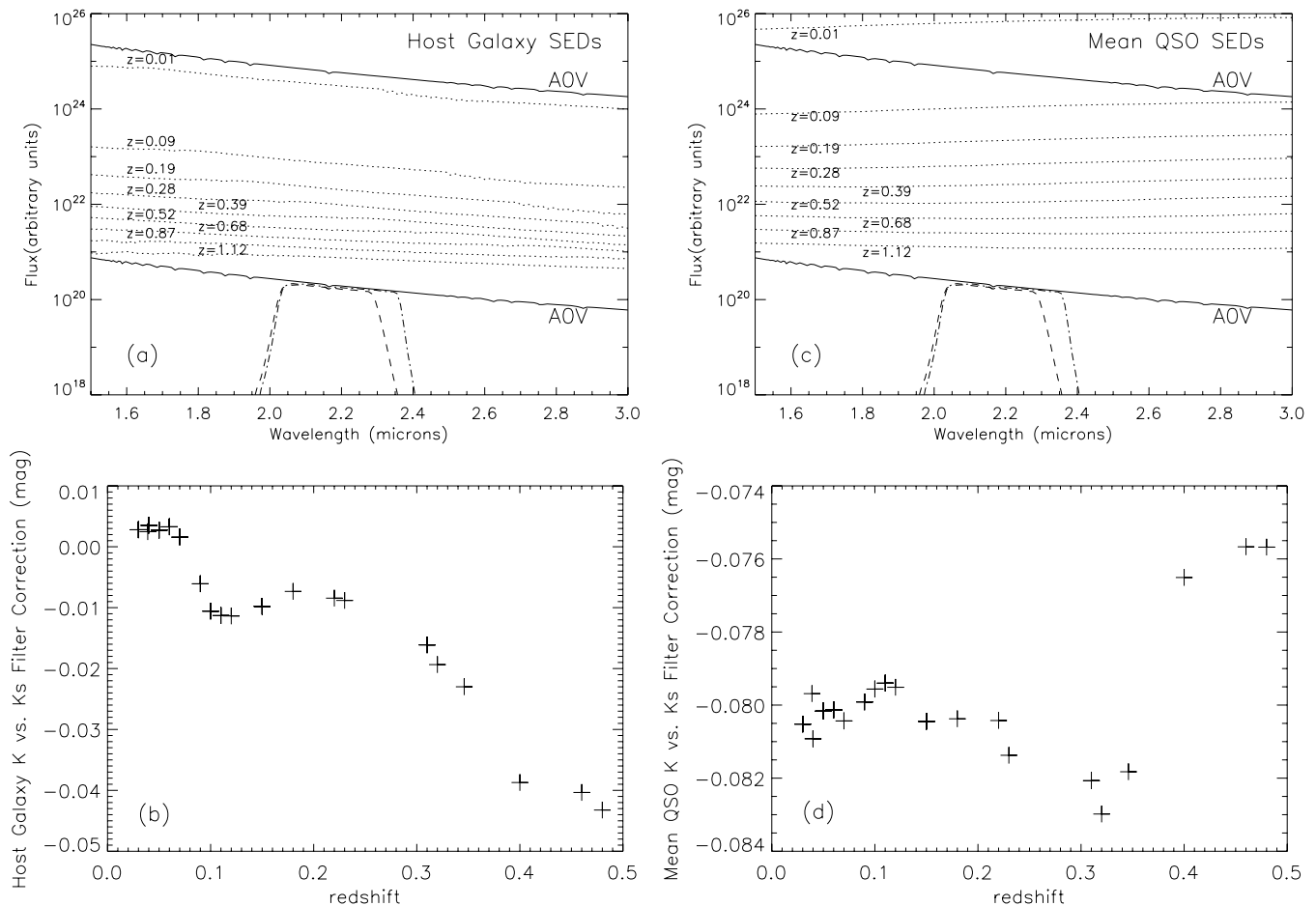


**Figure 1.** a, top left: filter profiles versus various SEDs, using the salpeter IMF solar metallicity models of Maraston et al. (2009), and assuming a red horizontal branch morphology. Dotted lines represent the SED of an elliptical galaxy formed at a redshift of 10 and observed at redshifts ranging from 0.01 to 1.12, with appropriate relative flux scaling. The solid lines display the spectral shape of the reference AOV star Vega. Dashed and dot-dashed lines display the  $K_S$ - and  $K$ -band filter profiles, respectively, after convolution with the lower AOV SED. At low redshifts, the spectral shapes of star and galaxy are comparable, while at higher redshifts the elliptical galaxy is significantly redder. This corresponds to a magnitude difference of effectively zero between  $K_S$ - and  $K$ -band observations of such a galaxy at  $z = 0$ , while at higher redshifts the omission of flux in the shorter  $K_S$  filter leads to a numerically larger value for magnitudes obtained in the  $K_S$  band. b, bottom left: plot of the difference between observed  $K_S$ - and  $K$ -band magnitudes for galaxies at the redshifts of our sample objects which were observed in the  $K_S$  filter; objects are generally brighter in the  $K$  band, except at the lowest redshifts. c, top right: filter profiles versus the redshifted mean QSO SED of Richards et al. (2006), with appropriate relative flux scaling. The reference AOV SED and filter profiles are as in frame (a). The spectral shape of the mean QSO SED is redder than that of the AOV reference star, and remains roughly constant over the redshift range of interest. d, bottom right: plot of the difference between observed  $K_S$ - and  $K$ -band magnitudes for a QSO at the redshifts of our sample objects which were observed in the  $K_S$  filter; a typical QSO at these redshifts would be brighter in the  $K$  band by roughly 0.08 mag.

band. We illustrate this effect in Fig. 1(a), which displays the SED of an elliptical galaxy formed at a redshift of 10 and observed at redshifts ranging from 0.01 to 1.12, alongside the two filter profiles and two scaled SEDs representative of Vega, which (in the Vega-based magnitude system) has a magnitude of zero in both bands. We have calculated the necessary numerical corrections which would need to be applied in order to convert a  $K_S$ -band magnitude to a  $K$ -band magnitude at the redshifts of all sources observed in the  $K_S$  filter; these values are displayed in Fig. 1(b). We also apply these  $K$ -corrections to the cleaned 64 kpc aperture photometry (Table 3, Column 6), producing a consistent set of  $K$ -band magnitudes for the whole sample (Table 3, Column 7). Also displayed in Figs 1(c) and (d) are similar plots illustrating the  $K$ -corrections which would be applicable to the mean SED of a quasar (from Richards et al. 2006) at the same redshifts of interest; these allow us to account for the minimal  $K$ -corrections of any modelled quasi-stellar object (QSO) point source components found in the  $K_S$ -band data.

## 4 RESULTS

The results of our aperture photometry, carried out as described in Section 3.1, are tabulated in Table 3. The errors on our final  $K$ -corrected magnitudes range from 1.5 to 12 per cent, and for over 70 per cent of our sample the photometric error is below 5 per cent. In addition to photometry we have also modelled the morphological properties of the sample galaxies, as detailed in the following sections.

### 4.1 GALFIT modelling

#### 4.1.1 Initial considerations

The aim of our modelling is not solely to derive an accurate model for each galaxy, but also one which is useful in a wider sense, allowing us to compare sources both within the sample and in the

wider literature in a simple, consistent and transparent manner. In brief, our modelling process asks the following questions: how well can the host galaxy be described as (A) a pure de Vaucouleurs elliptical [i.e. a galaxy with an  $n = 4$ ; Sérsic (1968) profile<sup>1</sup>], (B) a combination of de Vaucouleurs elliptical and an unresolved nuclear point source, and (C) a combination of an alternative Sérsic index profile and a nuclear point source, or more complex models as required. Our modelling utilizes GALFIT<sup>2</sup> (Peng et al. 2002, version 3.0 Peng et al. 2010), a well-documented two-dimensional fitting algorithm which allows the user to simultaneously fit a galaxy image with an arbitrary number of different model components, and thus to extract structural parameters of the galaxy. The model galaxy is convolved with a point spread function (PSF) and, using the downhill-gradient Levenberg–Marquardt algorithm, is matched to the observational data via the minimization of the  $\chi^2$  statistic.

As the data for some objects have been obtained over the course of several nights and with different observing conditions, the PSF for the combined data can be rather complex. We therefore derive point spread profiles for each object by extracting 2D images of stars in the field of view of each source, normalizing to unit flux and taking an average profile weighted by the signal-to-noise ratio of the component extracted stellar profiles. Where the resulting PSF data are still relatively noisy (i.e. for approximately half of our sources), we then use GALFIT to model the PSF as a combination of Gaussian functions, resulting in a less noisy PSF image with the same characteristic shape and full width at half-maximum (FWHM). This process results in an appropriate, high-quality PSF for each of our sample objects, regardless of the observing conditions or availability of bright stars in the field of view.

The host galaxies of our sample objects are modelled over an area equivalent to a  $100 \times 100 \text{ kpc}^2$  box on the plane of the sky at the redshift of the source in question. Alongside the morphological parameters of the host galaxy, our GALFIT modelling is also intended to determine the percentage contamination by any unresolved nuclear point source emission from the AGN. As demonstrated by Pierce et al. (2010), even a low level of AGN contamination can substantially affect the derived morphological parameters if it is left unaccounted for. As our data span a wide range of magnitudes and spatial resolutions, it is also important to consider how well we can disentangle nuclear point source emission from that of the host galaxy, particularly in cases of poor seeing. Is the fitting biased towards identifying higher or lower nuclear point source contributions, under the conditions of different host galaxy sizes, different magnitudes and spatial resolutions?

In order to address this question, it is important to understand how reliably GALFIT can extract morphological information from an image. This issue has been tested both by comparing GALFIT with other software and via the analysis of simulated data. For example, Floyd et al. (2008) tested the results produced by GALFIT in comparison with those of 2DM (McLure et al. 1999; Floyd et al. 2004), which is optimized for the analysis of quasars. Both routines produced very consistent results, though the error treatment of the latter was deemed better for sources dominated by their nuclear emission, and overall GALFIT’s separation of the extended host

galaxy emission from genuine unresolved emission from the galaxy nucleus was deemed to be very reliable. This result is backed up by our prior modelling of several sources in the sample, which used our own least-squares fitting routines, also based on the Levenberg–Marquardt algorithm. For PKS 2250–41 (Inskip et al. 2008) and PKS 1932–46 (Inskip et al. 2007), the structural parameters derived with GALFIT are in very close agreement with those determined for our previous work.

A number of different groups [primarily working with *Hubble Space Telescope* (HST) data] have used extensive sets of simulated images to test the performance of GALFIT (e.g. Sánchez et al. 2004; Jahnke et al. 2004; Simmons & Urry 2008; Kim et al. 2008; Gabor et al. 2009). In general, the magnitudes of bright point sources are very accurately recovered, although the morphological parameters of the host galaxies of such high-contrast systems were found to be less accurately constrained. However, spurious point-source contributions were identified in a small number of bulge-dominated systems (Simmons & Urry 2008). Such issues are in part due to PSF undersampling and/or mismatches (e.g. Kim et al. 2008), and the fact that the ACS (Advanced Camera for Surveys) PSF follows roughly an  $r^{1/4}$  profile (Jahnke et al. 2004). In cases where the PSF and galaxy data are well sampled, GALFIT accounts for observational PSFs very robustly (Peng et al. 2002, 2010; GALFIT website; Kim et al. 2008), and the size of the observational PSF has no significant impact on the further separation of host galaxy from nuclear point source. In the rest frame of our target objects, the physical resolution of our observations ranges from  $\sim 0.04 \text{ kpc}$  per pixel at best down to a minimum of  $1.3 \text{ kpc}$  per pixel for the highest redshift object in our sample. For our worst-resolution object (PKS 0023–26), the seeing FWHM is equivalent to a spatial scale of  $\sim 3.1 \text{ kpc}$ , and the host galaxy is clearly well resolved beyond this level. For our sample as a whole, undersampling of the host galaxy model components is not an issue, nor is undersampling of our PSF images, even for our large-field SOFI observations.

#### 4.1.2 Details of the modelling strategy

The free parameters for our most basic model (case A) are therefore the host galaxy centroid, its luminosity, scalelength (effective radius  $r_{\text{eff}}$ ), the position angle of its major axis ( $\theta$ ) and its ellipticity ( $b/a$ ). For case B, we add a further three free parameters, two for the centroid of the nuclear point source emission (which is not always precisely aligned with that of the host galaxy) and another for its luminosity. At this stage the observations have already been background-subtracted, and no background emission pedestal value was used initially. Once a good fit was obtained, we also allowed the residual background level to vary as an additional free parameter (within the constraints imposed by the residual background flux measured across the full field of view of our data), and in general this rarely led to any variation in the results obtained. For objects in crowded fields, we also iteratively model any neighbouring stars or galaxies which interfere with the host galaxy model fit; once a good model for these adjacent objects has been obtained, their parameters are held fixed, effectively removing them from consideration. Final reduced- $\chi^2$  values are determined by holding the fit values fixed and then modelling all other objects in the field of view; as the reduced- $\chi^2$  value is sensitive to the total residual flux as well as to the estimated value of the noise level in the data, the presence of companion objects would skew the resultant reduced- $\chi^2$  away from an ideal value of 1.0. For several sources (PKS 0043–42, PKS 0453–20, PKS 1934–63) the large values of the reduced

<sup>1</sup>The Sérsic surface brightness profile has the form  $\Sigma(r) = \Sigma_{\text{eff}} e^{-\kappa[(r/r_{\text{eff}})^{1/n} - 1]}$ , where  $\Sigma(r)$  is the surface brightness at a radius of  $r$ ,  $n$  is the Sérsic index,  $\kappa$  is a numerical parameter which varies with  $n$ ,  $r_{\text{eff}}$  is the effective radius of the galaxy (within which is contained half the light) and  $\Sigma_{\text{eff}}$  is the surface brightness at the effective radius.

<sup>2</sup><http://users.obs.carnegiescience.edu/peng/work/galfit/galfit.html>

$-\chi^2$  are due to the presence of unmodelled faint close companion objects, rather than denoting a poor fit to the host galaxy itself.

For our more complex model fits (case C), we consider a range of different Sérsic indices, and identify the best model resulting from the possible values of  $n = 1, 2, 4$  or  $6$ . While it would be possible to allow the Sérsic index  $n$  to vary freely, in general there is some level of degeneracy between the nuclear point source contribution and the Sérsic index (and to a lesser extent the background level and galaxy scalelength). By holding  $n$  fixed over an appropriate range of values, although we may overlook the ‘numerical best-fit’, we can more reliably obtain solid values for the other model parameters and a measure of the goodness of fit in each case. This also gives us a better understanding of how the source deviates from a more standard model which can be easily contrasted with other sources and previous models of the same galaxy within the literature. Where the galaxy is obviously more complex than a single Sérsic profile plus a point source, we also add further components; these are noted separately on a case-by-case basis. Finally, following the work of Donzelli et al. (2007) we also attempt to fit each source with a combination of an  $n = 4$  Sérsic bulge with an  $n = 1$  Sérsic disc component; unlike Donzelli et al., we fix the Sérsic parameter of the bulge at  $n = 4$  and also explicitly account for a nuclear point source component as an additional optional parameter of our modelling, as opposed to excluding the innermost point source contaminated regions from the model fits.

The results of our modelling are tabulated in Table 4, where we include the relevant values for the pure  $n = 4$  models (with and without a nuclear point source) and also the best-fitting models with alternative values of  $n$  and/or the Donzelli-style bulge/disc combination where appropriate. The modelling results are also presented pictorially in Figs 2–8; machine readable images can be obtained from the main 2 Jy website.<sup>3</sup> We display contour plots of only the central  $50 \text{ kpc} \times 50 \text{ kpc}$  part of this modelled region in Figs 2–8(a), together with contours of the best-fitting model (as denoted by the bold reduced- $\chi^2$  values in Table 4) overlaid on a grey-scale of the model-subtracted residual images in the same region. The choice of displaying only the central area of our modelled regions was made as it provides a far clearer illustration of the match between observation and model, and any residual features observed. In the following section, we provide more detailed notes on the results obtained for each individual object.

## 4.2 Notes on individual objects

In this section, we present notes on each individual object in turn. Where comparisons are made with other morphological modelling studies in the literature, these all account for the presence of a nuclear point source component, except where otherwise noted.

### 4.2.1 PKS 0023–26

PKS 0023–26, at a redshift of  $z = 0.322$ , is one of the higher redshift objects in our sample. The source appears to lie within a dense cluster environment: VLT spectroscopy has shown that the two neighbouring galaxies to either side (at the edges of the frame in Fig. 2a) lie at the same redshift (RA10; Tadhunter et al., in preparation).

Our GALFIT modelling of this source is consistent with a de Vaucouleurs elliptical, though there is considerable degeneracy between effective radius and the Sérsic index for this source owing to the lower signal-to-noise ratio and smaller spatial scale. For fits with  $n = 4$ , we find  $r_{\text{eff}} = 1.0 \text{ arcsec}$  ( $\sim 5 \text{ kpc}$ ) for fits without a point source, and  $r_{\text{eff}} = 4.4 \text{ arcsec}$  ( $\sim 20 \text{ kpc}$ ) with a best-fitting unresolved nuclear point source contribution of 12.2 per cent. The large effective radius in this case is not unrealistic; deeper  $r'$ -band imaging observations of this source (Tadhunter et al. 2010) reveal that it lies at the centre of a cluster and is surrounded by a large diffuse halo which extends out to projected distances at least as far as the two neighbouring objects in the field.

### 4.2.2 PKS 0034–01 (3C15)

For this source, our best-fitting model is a de Vaucouleurs elliptical with an effective radius of  $3.7 \text{ arcsec}$  ( $\sim 5 \text{ kpc}$ ), and a point source contribution of  $\sim 4$  per cent. By comparison,  $R$ -band observations and  $r^{1/4}$  modelling of this source by Govoni et al. (2000) found a larger effective radius of  $6.3 \text{ arcsec}$ . Zirbel (1996) records an even larger effective radius of  $6.9 \text{ arcsec}/9.1 \text{ kpc}$  (after conversion to our assumed cosmological model, and with no nuclear point source component) at even bluer (observed  $V$  band) wavelengths. However, Fasano, Falomo & Scarpa (1996) find a more comparable effective radius ( $5.24 \text{ arcsec}$ ), also in the  $R$  band. At infrared wavelengths,  $H$ -band NICMOS observations (Floyd et al. 2008) also find very similar values to our own ( $r_e = 4.96 \pm 0.45 \text{ kpc}$  with  $n = 4.17$ ).

Interestingly, an optical synchrotron jet has been observed in this source (Martel et al. 1998) at a position angle of  $-30^\circ$ . We also observe this feature in the  $K_S$  band, visible both in the  $K_S$ -band contour plot (Fig. 2c) and our model-subtracted residual image (Fig. 2d). Martel et al. (1998) and Sparks et al. (2000) also observe complex emission and dust features in the nuclear region of PKS 0034–01. The complex nuclear residuals present in our data could potentially be the same features, although we cannot rule out small-scale PSF variations as the cause in this case.

### 4.2.3 PKS 0035–02 (3C17)

Our modelling of this source gives a best fit  $r_{\text{eff}} = 7.64 \text{ kpc}$  ( $2.17 \text{ arcsec}$ ) with a Sérsic index of  $n = 4$ , and a nuclear point source contribution of 23.9 per cent, consistent with its status as a BLRG. Our derived galaxy effective radius is a little larger than that found by Floyd et al. (2008) in their study of NICMOS observations of this source, and roughly twice that determined at the same wavelength range by Tremblay et al. (2007) and Donzelli et al. (2007), though this is likely due to the smaller Sérsic index of  $n \sim 2.7$  used by the latter. Our derived radius is smaller than the  $10 \text{ kpc}$  value found in the optical de Vaucouleurs-only modelling of Zirbel (1996). Our model residuals display an excess of flux extending linearly to the NE–SW (aligned with the galaxy major axis in optical WFPC2 data; de Koff et al. 1996), with a slight oversubtraction in the region immediately beyond this excess flux. Beyond this, we observe subtle variations in the background emission surrounding a number of fainter features/companion objects lying close to the host galaxy. It is possible that these features have biased our model towards a larger effective radius, and it should be noted that a secondary minimum in our modelling is observed at a similar effective radius to that found for the zero-point source model.

PKS 0035–02 has a very interesting radio morphology (Morganti et al. 1999). The south-eastern radio jet displays an

<sup>3</sup> <http://2jy.extragalactic.info>

**Table 4.** Results of GALFIT3.0 modelling of the 2 Jy host galaxies. For the Sersic models used, each line gives the Sersic index (or indices) used ( $n$ ), the magnitude of the Sersic component(s), the percentage contribution of any nuclear point source emission to the *total* model galaxy flux and the effective radius of the Sersic component(s) in both arcsec and kiloparsec in the rest frame of the host galaxy. The reduced  $\chi^2$  of the model is given in the final column (and includes the effect of fitting the majority of other bright objects in the fitting field of view); bold font for this value indicates that this model is the one used in the production of the images displayed in Figs 2–8.

Source	Sersic $n$	$M_{\text{gal}}$	Point source (per cent)	$R_{\text{eff}}$ (arcsec)	$R_{\text{eff}}$ (kpc)	reduced $\chi^2$
PKS 0023–26	4	15.76	–	1.02 ± 0.05	4.74 ± 0.26	1.049
	4	15.35	12.3 ± 0.5	4.20 ± 0.32	19.47 ± 1.48	<b>0.9278</b>
PKS 0034–01	4	13.13	–	2.59 ± 0.13	3.56 ± 0.18	1.344
	4	13.05	4.3 ± 0.1	3.71 ± 0.19	5.09 ± 0.26	<b>1.321</b>
PKS 0035–02	4	14.25	–	0.59 ± 0.03	2.06 ± 0.10	1.053
	4	14.22	23.5 ± 0.3	2.17 ± 0.11	7.64 ± 0.39	<b>0.9059</b>
PKS 0038+09	4	14.45	–	0.10 ± 0.01	0.31 ± 0.02	1.135
	4	15.33	63.3 ± 0.7	1.77 ± 0.11	5.53 ± 0.33	<b>1.062</b>
PKS 0039–44				Too faint/low S/N to model		
PKS 0043–42	4	13.28	–	1.89 ± 0.10	3.92 ± 0.20	1.618
	4	13.11	10.8 ± 0.2	4.35 ± 0.24	9.04 ± 0.49	<b>1.449</b>
PKS 0055–01	4	11.26	–	11.46 ± 0.61	10.00 ± 0.53	1.282
				No adequate fit for $n = 4 + \text{point source}$		
PKS 0105–16	1	11.81	1.2 ± 0.1	4.65 ± 0.24	4.06 ± 0.21	<b>1.243</b>
	4	15.37	–	0.73 ± 0.04	3.89 ± 0.21	1.284
	4	15.89	32.6 ± 1.1	1.20 ± 0.10	6.45 ± 0.55	<b>1.045</b>
PKS 0131–36	4	9.28	–	16.39 ± 0.82	9.72 ± 0.49	2.491
				No adequate fit for $n = 4 + \text{point source}$		
PKS 0213–132	4+edge-on disc <sup>1</sup>	9.41	–	20.25 ± 1.01	12.01 ± 0.60	<b>1.174</b>
	4	14.51	–	1.54 ± 0.09	3.91 ± 0.24	1.062
	4	14.22	10.0 ± 0.8	4.31 ± 0.41	10.97 ± 1.05	<b>1.053</b>
PKS 0305+03	4	8.87	–	17.31 ± 0.87	10.26 ± 0.51	0.9969
	4	8.82	1.0 ± 0.1	19.70 ± 0.99	11.68 ± 0.59	0.9866
	6	8.44	0	37.62 ± 1.88	22.31 ± 1.12	0.9844
PKS 0325+02	4,1 (bulge+disc) <sup>2</sup>	8.78,12.99	0 <sup>2</sup>	21.76 ± 1.09, 1.11 ± 0.06	12.90 ± 0.65, 0.66 ± 0.03	<b>0.9829</b>
	4	9.89	–	28.05 ± 1.41	16.63 ± 0.83	1.039
	4	9.77	0.7 ± 0.1	34.17 ± 1.73	20.26 ± 1.02	1.033
	6	9.22	0.2 ± 0.1	81.67 ± 4.17	48.43 ± 2.47	1.031
PKS 0347+05 (RG, extra, QSO)	4,1 (bulge+disc) <sup>2</sup>	10.79, 10.95	0.3 ± 0.2 <sup>2</sup>	12.53 ± 0.67, 29.85 ± 1.55	7.43 ± 0.40, 17.70 ± 0.92	<b>1.029</b>
	4, 4, 6	14.28, 17.53, 15.46	–, –, 19.6 ± 0.4	1.77 ± 0.09, 0.29 ± 0.02, 1.73 ± 0.11	8.50 ± 0.43, 1.42 ± 0.11, 8.32 ± 0.55	<b>0.8046</b>
PKS 0349–27	4	13.12	–	1.86 ± 0.09	2.33 ± 0.12	1.294
	4	12.87	10.7 ± 0.1	5.33 ± 0.27	6.66 ± 0.34	1.081
	6	12.60	7.0 ± 0.1	8.04 ± 0.42	10.05 ± 0.52	<b>1.072</b>
PKS 0404+03	4	13.62	–	1.81 ± 0.09	2.98 ± 0.15	1.103
	4	13.57	6.4 ± 0.1	2.69 ± 0.14	4.41 ± 0.22	1.039
PKS 0427–53 (east, <sup>3</sup> west)	4,1 (bulge+disc) <sup>2</sup>	14.05,14.68	3.2 ± 0.1 <sup>2</sup>	1.35 ± 0.07, 5.06 ± 0.26	2.22 ± 0.11, 8.29 ± 0.43	<b>0.991</b>
PKS 0430+05	4, 4	10.13 <sup>3</sup> , 11.32	–, –	12.02 ± 0.60 <sup>3</sup> , 7.00 ± 0.35	9.61 ± 0.48 <sup>3</sup> , 5.59 ± 0.28	<b>0.8667</b>
	4	10.73	–	0.38 ± 0.02	0.24 ± 0.02	2.004
	4	10.75	39.1 ± 0.4	6.48 ± 0.33	4.21 ± 0.21	1.698
PKS 0442–28	4,1 (bulge+disc) <sup>2</sup>	10.64,12.79	33.0 ± 0.3 <sup>2</sup>	13.27 ± 0.68, 0.96 ± 0.05	8.62 ± 0.44, 0.62 ± 0.03	<b>1.681</b>
	4	13.44	–	0.73 ± 0.04	1.85 ± 0.09	5.246
	4	13.14	23.5 ± 0.4	5.96 ± 0.34	15.14 ± 0.87	<b>3.611</b>

Table 4 – continued

Source	Sersic $n$	$M_{\text{gal}}$	Point source (per cent)	$R_{\text{eff}}$ (arcsec)	$R_{\text{eff}}$ (kpc)	reduced $\chi^2$
PKS 0453–20	4	9.65	–	23.19 ± 1.17	15.93 ± 0.80	2.668
PKS 0518–45	4	9.63	0.2 ± 0.1	23.98 ± 1.21	16.47 ± 0.83	<b>2.666</b>
PKS 0521–36	4	12.33	41.3 ± 0.4	No adequate fit for $n = 4$	7.31 ± 0.37	1.321
	2	12.69	49.8 ± 0.5	10.64 ± 0.54	4.51 ± 0.23	<b>1.287</b>
	4	11.59	48.2 ± 0.5	No adequate fit for $n = 4$	4.53 ± 0.23	1.491
	2	11.88	56.2 ± 0.6	4.30 ± 0.22	3.70 ± 0.19	1.458
	4,1 (bulge+disc) <sup>2</sup>	11.88, 12.93	49.1 ± 0.5 <sup>2</sup>	3.50 ± 0.18	11.92 ± 0.61, 2.41 ± 0.12	<b>1.316</b>
PKS 0625–53 (east, <sup>4</sup> west)	4, 4	9.62 <sup>4</sup> , 11.01	–, –	11.28 ± 0.58, 2.28 ± 0.11	24.50 ± 1.23 <sup>4</sup> , 6.90 ± 0.34	0.7766
	4, 4	9.61, 10.94	0.2 ± 0.2, 1.2 ± 0.1	23.62 ± 1.19 <sup>4</sup> , 6.65 ± 0.33	24.95 ± 1.25, 7.92 ± 0.40	<b>0.7624</b>
PKS 0625–35	4	10.81	–	24.06 ± 1.20, 7.64 ± 0.38	4.81 ± 0.24	3.612
	4	10.56	7.3 ± 0.1	4.56 ± 0.23	10.06 ± 0.05	1.964
	4	10.46, 12.86	6.8 ± 0.1 <sup>2</sup>	9.53 ± 0.48	19.80 ± 1.03, 2.28 ± 0.12	<b>1.893</b>
PKS 0806–10	4	12.41	–	18.77 ± 0.98, 2.16 ± 0.11	2.01 ± 0.10	1.910
PKS 0859–25	4	12.18	20.5 ± 0.3	1.02 ± 0.05	9.51 ± 0.49	<b>1.196</b>
	4	14.75	–	4.81 ± 0.25	6.12 ± 0.32	0.8891
	4	14.55	7.2 ± 5.8	1.37 ± 0.07	12.02 ± 0.73	<b>0.8550</b>
PKS 0915–11	4, 4	10.09, 13.49	–	2.69 ± 0.16	28.39 ± 1.42, 0.71 ± 0.04	0.4475
	2, 4	10.45, 13.49	–	27.38 ± 1.37, 0.68 ± 0.03	16.33 ± 0.84, 0.71 ± 0.04	0.476
PKS 0945+07	2, 0.64, 4	10.55, 13.45, 13.49	–	No adequate fit for $n = 4$ + point source	16.45 ± 0.82, 1.86 ± 0.09, 0.71 ± 0.04	<b>0.2091</b>
	4	13.14	56.9 ± 0.6	15.75 ± 0.81, 0.68 ± 0.03		
PKS 1306–09 <sup>5</sup>	4	14.96	–	No adequate fit for $n = 4$	11.88 ± 0.64	<b>1.240</b>
	4	14.94	20.9 ± 0.2 <sup>5</sup>	7.46 ± 0.40	4.98 ± 0.25	1.325
PKS 1547–79	4	15.82, 17.43	–	0.85 ± 0.04	13.55 ± 0.71	<b>0.8829</b>
	1, 4	15.50, 17.43	29.2 ± 3.1, 0	2.32 ± 0.12		
	4, 4		3.2 <sup>+12.9</sup> <sub>–3.2</sub> , 0	No adequate fit for $n = 4$ with point source = 0	5.97 ± 0.38, 16.89 ± 1.89	0.3350
PKS 1549–79	4	13.66	71.5 ± 0.7	0.87 ± 0.06, 2.83 ± 0.32	7.46 ± 0.44, 16.89 ± 1.89	<b>0.3358</b>
	2	13.93	76.8 ± 0.8	1.25 ± 0.07, 2.83 ± 0.32		
PKS 1559+02	1	14.16	80.7 ± 0.8	No adequate fit for $n = 4$ with point source = 0	10.80 ± 0.55	1.405
	4	11.92	–	4.17 ± 0.21	8.89 ± 0.45	1.324
	4	11.87	0.9 ± 0.1	3.44 ± 0.17	8.09 ± 0.41	<b>1.279</b>
	6	11.46	–	3.13 ± 0.16	12.13 ± 0.61	0.8753
PKS 1733–56 <sup>6</sup>	4	12.60	–	6.39 ± 0.32	13.56 ± 0.68	0.8657
	4	12.57	13.3 ± 0.2	7.14 ± 0.36	23.87 ± 1.20	<b>0.8586</b>
PKS 1814–63	4	12.18	–	14.25 ± 0.71	3.55 ± 0.18	1.165
	4	12.25	15.0 ± 0.2	1.99 ± 0.10	6.61 ± 0.33	<b>1.045</b>
	2	12.52	25.4 ± 0.3	3.89 ± 0.20	2.76 ± 0.14	1.581
PKS 1932–46	4	15.06	–	2.31 ± 0.12	5.20 ± 0.26	1.449
	4	14.95	15.2 ± 0.3	4.35 ± 0.22	5.13 ± 0.26	<b>1.433</b>
PKS 1934–63 (east, <sup>7</sup> west)	4, 2	14.44 <sup>7</sup> , 15.36	– <sup>7</sup> , 7.0 ± 0.7	0.88 ± 0.05	3.18 ± 0.17	1.017
	4, 2	14.42, 15.41	4.6 ± 0.7, 6.6 ± 0.7	2.31 ± 0.14	8.38 ± 0.51	<b>0.9788</b>
PKS 1949+02	4	11.36	–	1.15 ± 0.06, <sup>7</sup> 2.08 ± 0.15	3.52 ± 0.19, <sup>7</sup> 6.36 ± 0.45	2.568
	4	11.29	5.0 ± 0.1	1.43 ± 0.09, 1.97 ± 0.14	4.38 ± 0.28, 5.99 ± 0.42	<b>2.567</b>
	4		–	4.51 ± 0.23	5.07 ± 0.26	2.156
	4		–	6.29 ± 0.31	7.08 ± 0.35	<b>1.955</b>

**Table 4** – *continued*

Source	Sérsic $n$	$M_{\text{gal}}$	Point source (per cent)	$R_{\text{eff}}$ (arcsec)	$R_{\text{eff}}$ (kpc)	Reduced $\chi^2$
PKS 2153–69	4	10.29	–	$8.45 \pm 0.42$	$4.69 \pm 0.23$	1.254
	4	10.07	$4.4 \pm 0.1$	$14.39 \pm 0.72$	$7.97 \pm 0.40$	1.116
	4.1 (bulge+disc) <sup>2</sup>	9.94, 13.23	$3.6 \pm 0.1^2$	$21.84 \pm 1.10, 1.51 \pm 0.08$	$12.09 \pm 0.61, 0.84 \pm 0.04$	<b>1.102</b>
PKS 2211–17	4	12.24	–	$19.03 \pm 0.95$	$50.03 \pm 2.51$	<b>0.5733</b>
			No adequate fit for $n = 4$ + point source			
PKS 2221–02	4	12.17	–	$0.003^{+0.06}_{-0.003}$	$0.004^{+0.08}_{-0.004}$	1.830
	4	12.40	$64.7 \pm 0.7$	$7.02 \pm 0.41$	$7.53 \pm 0.44$	<b>1.505</b>
PKS 2250–41	4	15.60	–	$0.44 \pm 0.02$	$1.98 \pm 0.11$	1.045
	4	15.63	$16.6 \pm 0.7$	$1.09 \pm 0.07$	$4.88 \pm 0.33$	<b>1.040</b>
PKS 2314+03	4	13.90	–	$0.35 \pm 0.02$	$1.23 \pm 0.06$	1.612
	4	13.74	$35.9 \pm 0.4$	$5.74 \pm 0.31$	$20.18 \pm 1.09$	<b>1.068</b>
PKS 2356–61	4	12.40	–	$4.66 \pm 0.23$	$8.19 \pm 0.41$	0.9418
	4	12.36	$2.4 \pm 0.1$	$5.56 \pm 0.28$	$9.77 \pm 0.49$	<b>0.9037</b>

*Notes.* [1] Best-fitting model for PKS 0131–36 includes an edge on disc with a central surface brightness of  $14.81 \text{ mag arcsec}^{-2}$ , a scaleheight of  $1.2 \text{ arcsec}$  and a scalelength of  $3.4 \text{ arcsec}$ .

[2] Point source is given as percentage of total (bulge+disc+point source) galaxy flux.

[3] The eastern galaxy of this pair is the radio source host.

[4] The eastern galaxy of this pair is the radio source host.

[5] Point source centroid offset from galaxy centroid by  $\sim 0.5 \text{ arcsec}$ .

[6] Companion modelled as  $K = 16.15$  point source.

[7] The eastern galaxy of this interacting pair is the radio source host.

extreme bend and a number of bright hotspots. Intriguingly, these structures appear to be almost perfectly aligned with the features observed in our  $K$ -band images.

#### 4.2.4 PKS 0038+09 (3C18)

Approximately two-thirds of the  $K$ -band flux from this source is modelled as an unresolved nuclear point source, consistent with PKS 0038+09's status as a BLRG. We find a de Vaucouleurs effective radius of  $\sim 5.5 \text{ kpc}$  ( $1.77 \text{ arcsec}$ ), slightly larger than the value measured in the  $V$  band for this source in the de Vaucouleurs-only modelling of Zirbel (1996). Considering alternative Sérsic indices, the model with  $n = 2$  provides a comparably good fit to the data, with an effective radius of  $4.85 \text{ kpc}$  ( $1.56 \text{ arcsec}$ ) and a nuclear point source contribution of 70 per cent.

#### 4.2.5 PKS 0043–42

PKS 0043–42 is a WLRG, which appears to be interacting with a companion object to the north. Three further objects lie to the south and north east at projected distances of  $\sim 17 \text{ arcsec}$ . Our best-fitting de Vaucouleurs model includes a nuclear point source contribution of the order of  $\sim 10$  per cent, and an effective radius of  $4.35 \text{ arcsec}/9 \text{ kpc}$ . It should be noted that the inner regions of this galaxy are rather complex, and there are other possible causes for the excess flux currently fitted by the point source. We observe a central isophotal twist and an E–W dimming/N–S excess flux, possibly due to a dust lane and/or excess flux associated with the apparent interaction.

#### 4.2.6 PKS 0055–01 (3C29)

Assuming a Sérsic index of  $n = 4$ , our measured effective radius for this source is  $11.46 \text{ arcsec}$  ( $10.00 \text{ kpc}$ ), comparable to those found in the previous  $R$ -band studies by Govoni et al. (2000), Fasano et al. (1996) and Smith & Heckman (1989) of  $9.7, 10.3$  and  $12.7 \text{ arcsec}$ , respectively.

However, our best-fitting model includes a very small nuclear point source contribution and a smaller ( $4.06 \text{ kpc}; 4.65 \text{ arcsec}$ ), disc-type Sérsic index of  $n = 1$ , with an excess of flux in the inner regions of the galaxy. This ties in with Fasano et al.'s comments on the shape of the luminosity profile of PKS 0055–01, which they find to be too bright in the centre to be explained by an exponential law, and too faint for a de Vaucouleurs law, and explain in terms of strong nuclear absorption. We confirm that the same luminosity profile is observed in our  $K_S$ -band data.

#### 4.2.7 PKS 0105–16 (3C32)

PKS 0105–16 is well fit by a de Vaucouleurs elliptical with  $r_{\text{eff}} = 6.5 \text{ kpc}$  and a  $K_S$ -band nuclear point source contribution of 32.6 per cent.

#### 4.2.8 PKS 0131–36 (NGC0612)

PKS 0131–36 has been previously classified as an S0 galaxy (Kotanyi & Ekers 1979; Sansom et al. 1987), and more recently as being well described by a de Vaucouleurs elliptical model (Fasano et al. 1996; Véron-Cetty & Véron 2001). It has a luminous near edge-on disc, which has a gaseous counterpart (Emonts et al. 2008),

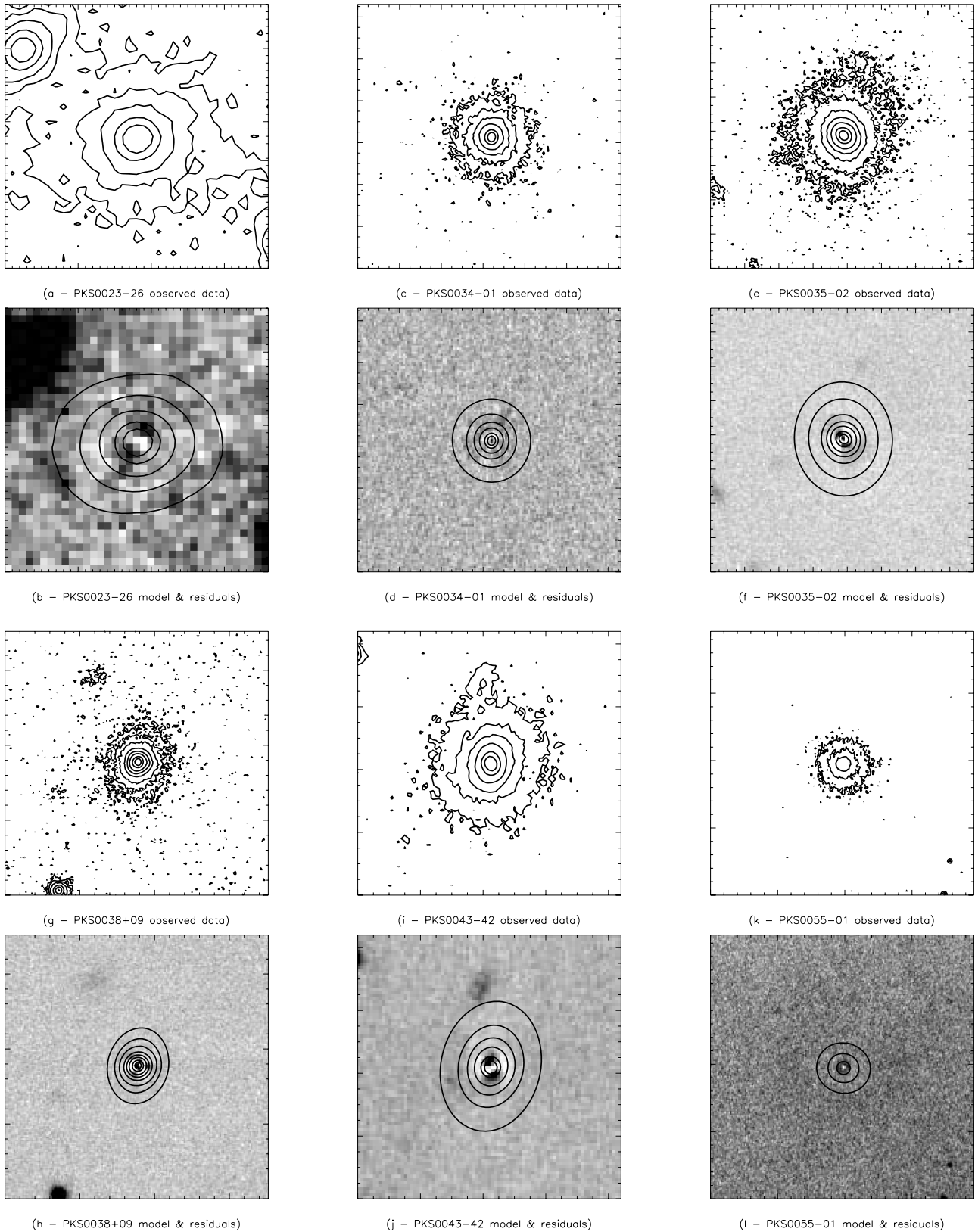


**Figure 2.** 50 kpc by 50 kpc images of PKS 0023–26, PKS 0034–01, PKS 0035–02, PKS 0038+09, PKS 0043–42 and PKS 0055–01. The observed data contours are displayed in frames (a), (c), (e), (g), (i) and (k), while frames (b), (d), (f), (h), (j) and (l) show the best-fitting model contours on grey-scale images of the model-subtracted residuals. The maximum contour level is 50 per cent of the peak flux for that source in all cases, with subsequent contours at 25 per cent, 10 per cent, 5 per cent, 2.5 per cent, 1 per cent, 0.5 per cent and 0.25 per cent (latter flux levels not shown in all cases). The minimum contours displayed are at 0.25 per cent for PKS 0038+09, 0.5 per cent for PKS 0035–02, 1 per cent for PKS 0034–01 and PKS 0043–42, 2.5 per cent for PKS 0023–26 and 10 per cent for PKS 0055–01.

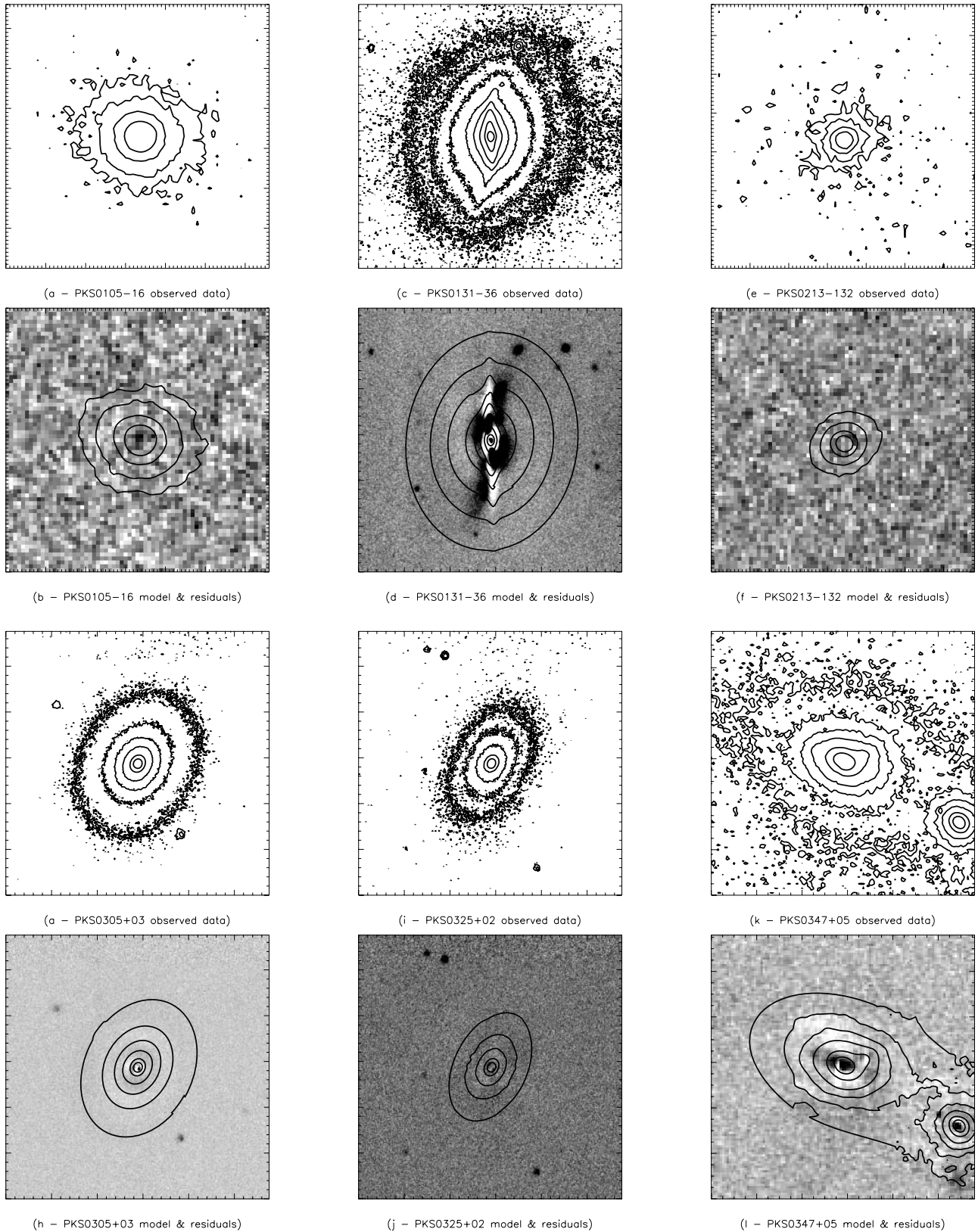


**Figure 3.** 50 kpc by 50 kpc images of PKS 0105-16, PKS 0131-36, PKS 0213-132, PKS 0305+03, PKS 0325+02 and PKS 0347+05. The observed data contours are displayed in frames (a), (c), (e), (g), (i) and (k), while frames (b), (d), (f), (h), (j) and (l) show the best-fitting model contours on grey-scale images of the model-subtracted residuals. The maximum contour level is 50 per cent of the peak flux for that source in all cases, with subsequent contours at 25 per cent, 10 per cent, 5 per cent, 2.5 per cent, 1 per cent, 0.5 per cent and 0.25 per cent (latter flux levels not shown in all cases). The minimum contours displayed are at 0.25 per cent for PKS 0131-36, 1 per cent for PKS 0305+03 and PKS 0347+05, 2.5 per cent for PKS 0325+02, and 5 per cent for PKS 0105-16 and PKS 0213-132.

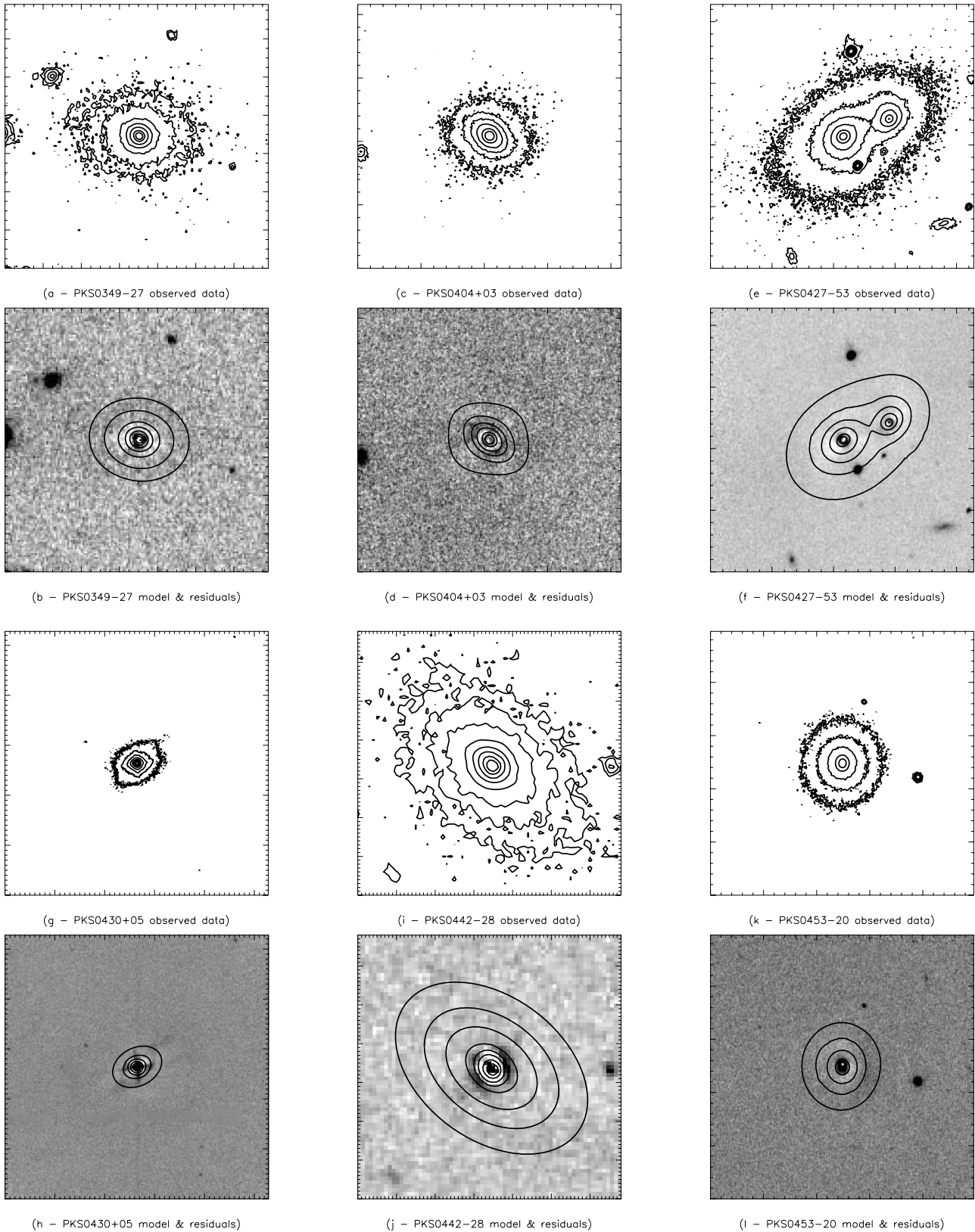


**Figure 4.** 50 kpc by 50 kpc images of PKS 0349-27, PKS 0404+03, PKS 0427-53, PKS 0430+05, PKS 0442-28 and PKS 0453-20. The observed data contours are displayed in frames (a), (c), (e), (g), (i) and (k), while frames (b), (d), (f), (h), (j) and (l) show the best-fitting model contours on grey-scale images of the model-subtracted residuals. The maximum contour level is 50 per cent of the peak flux for that source in all cases, with subsequent contours at 25 per cent, 10 per cent, 5 per cent, 2.5 per cent, 1 per cent, 0.5 per cent, 0.25 per cent and 0.1 per cent (latter flux levels not shown in all cases). The minimum contours displayed are at 0.1 per cent for PKS 0430+05, 0.25 per cent for PKS 0442-28, 0.5 per cent for PKS 0349-27, 1 per cent for PKS 0404+03 and PKS 0427-53, and 2.5 per cent for PKS 0453-20.

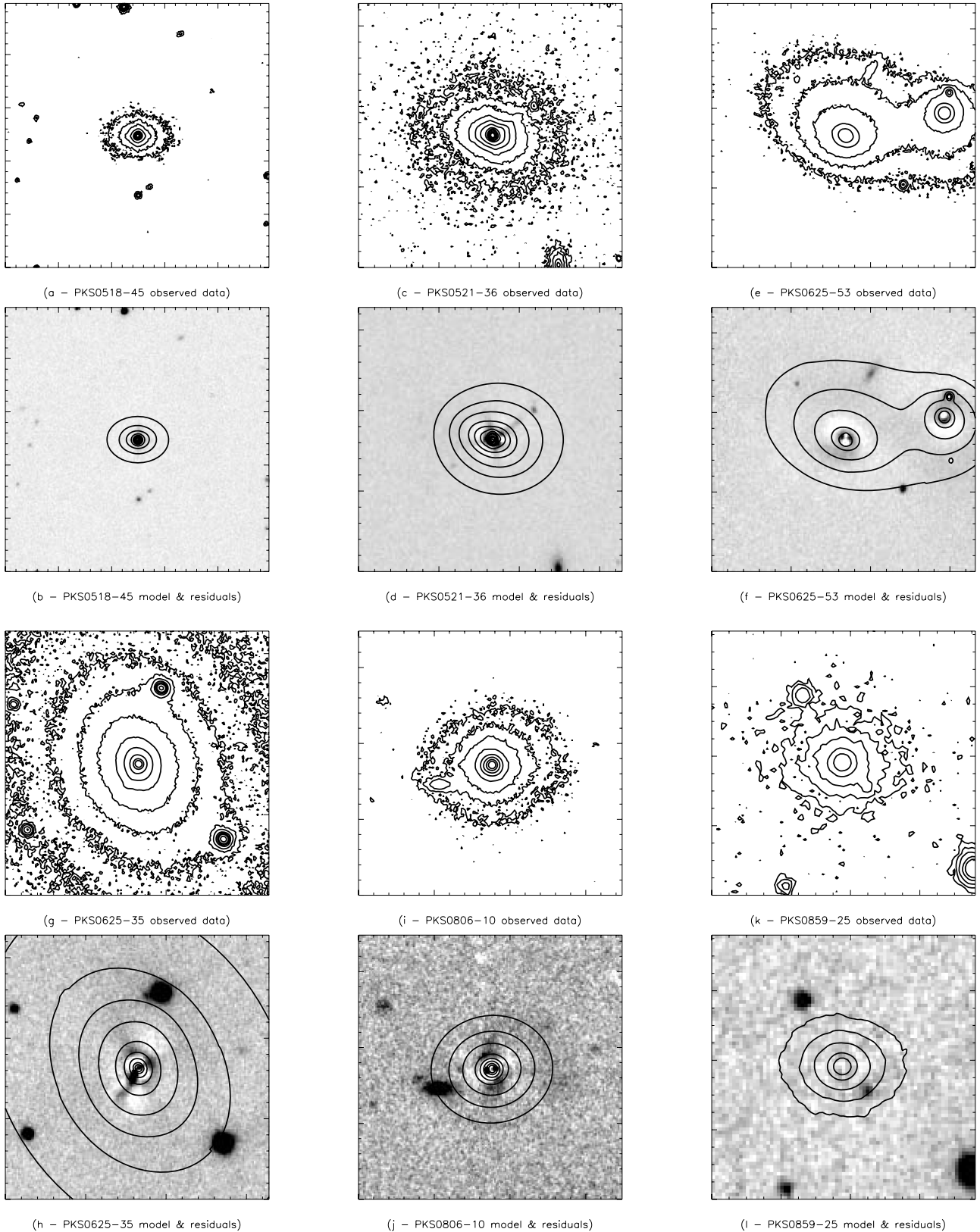


**Figure 5.** 50 kpc by 50 kpc images of PKS 0518–45, PKS 0521–36, PKS 0625–53, PKS 0625–35, PKS 0806–10 and PKS 0859–25. The observed data contours are displayed in frames (a), (c), (e), (g), (i) and (k), while frames (b), (d), (f), (h), (j) and (l) show the best-fitting model contours on grey-scale images of the model-subtracted residuals. The maximum contour level is 50 per cent of the peak flux for that source in all cases, with subsequent contours at 25 per cent, 10 per cent, 5 per cent, 2.5 per cent, 1 per cent, 0.5 per cent, 0.25 per cent, 0.1 per cent, 0.05 per cent and 0.025 per cent (latter flux levels not shown in all cases). The minimum contours displayed are at 0.025 per cent for PKS 0521–36, 0.1 per cent for PKS 0518–45 and PKS 0625–35, 0.25 per cent for PKS 0806–10, and 2.5 per cent for PKS 0625–53 and PKS 0859–25.

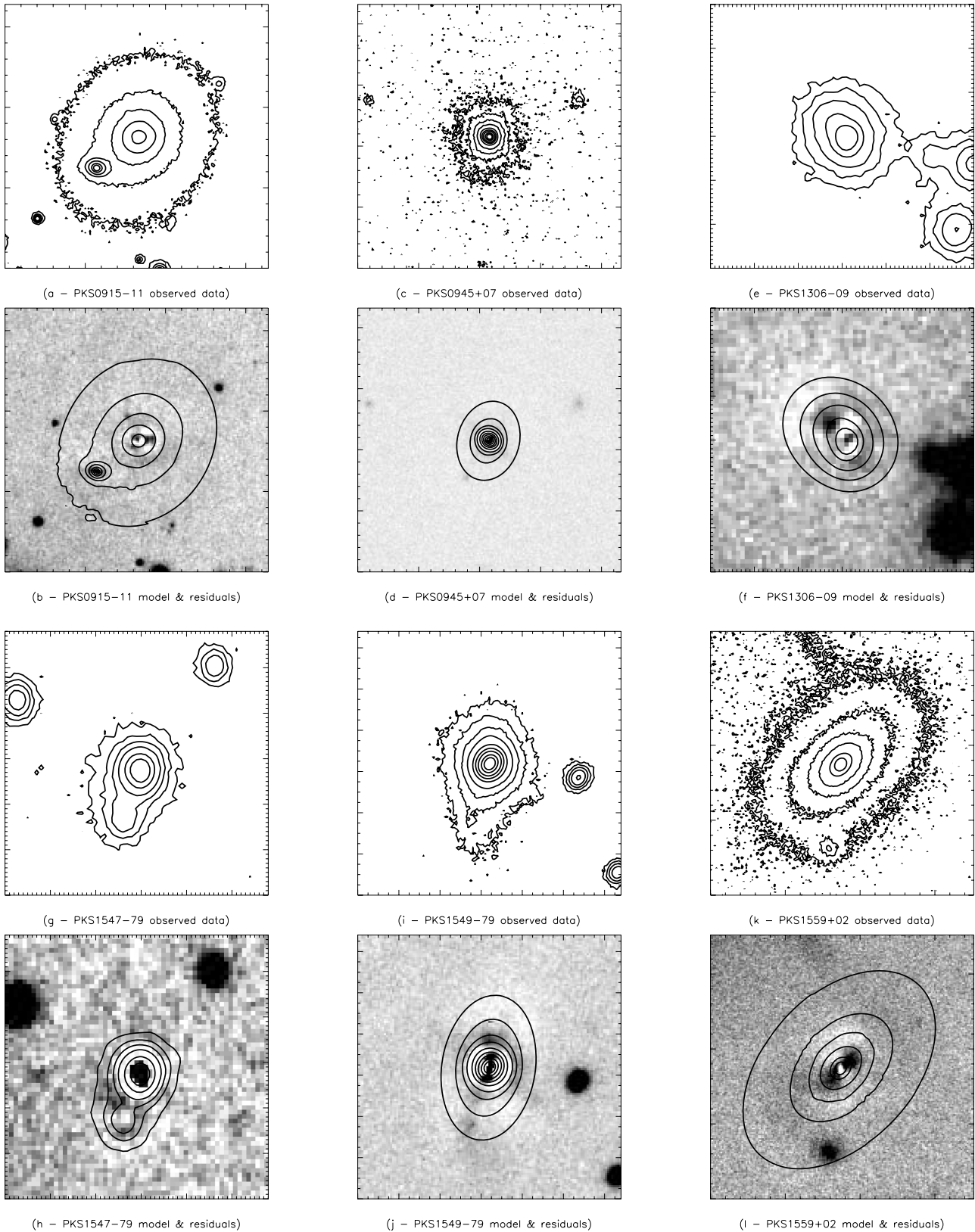


**Figure 6.** 50 kpc by 50 kpc images of PKS 0915-11, PKS 0945+07, PKS 1306-09, PKS 1547-79, PKS 1549-79 and PKS 1559+02. The observed data contours are displayed in frames (a), (c), (e), (g), (i) and (k), while frames (b), (d), (f), (h), (j) and (l) show the best-fitting model contours on grey-scale images of the model-subtracted residuals. The maximum contour level is 50 per cent of the peak flux for that source in all cases, with subsequent contours at 25 per cent, 10 per cent, 5 per cent, 2.5 per cent, 1 per cent, 0.5 per cent, 0.25 per cent and 0.1 per cent, (latter flux levels not shown in all cases). The minimum contours displayed are at 0.1 per cent for PKS 0945+07 and PKS 1549-79, 1 per cent for PKS 0915-11, PKS 1547-79 and PKS 1559+02, and 2.5 per cent for PKS 1306-09.

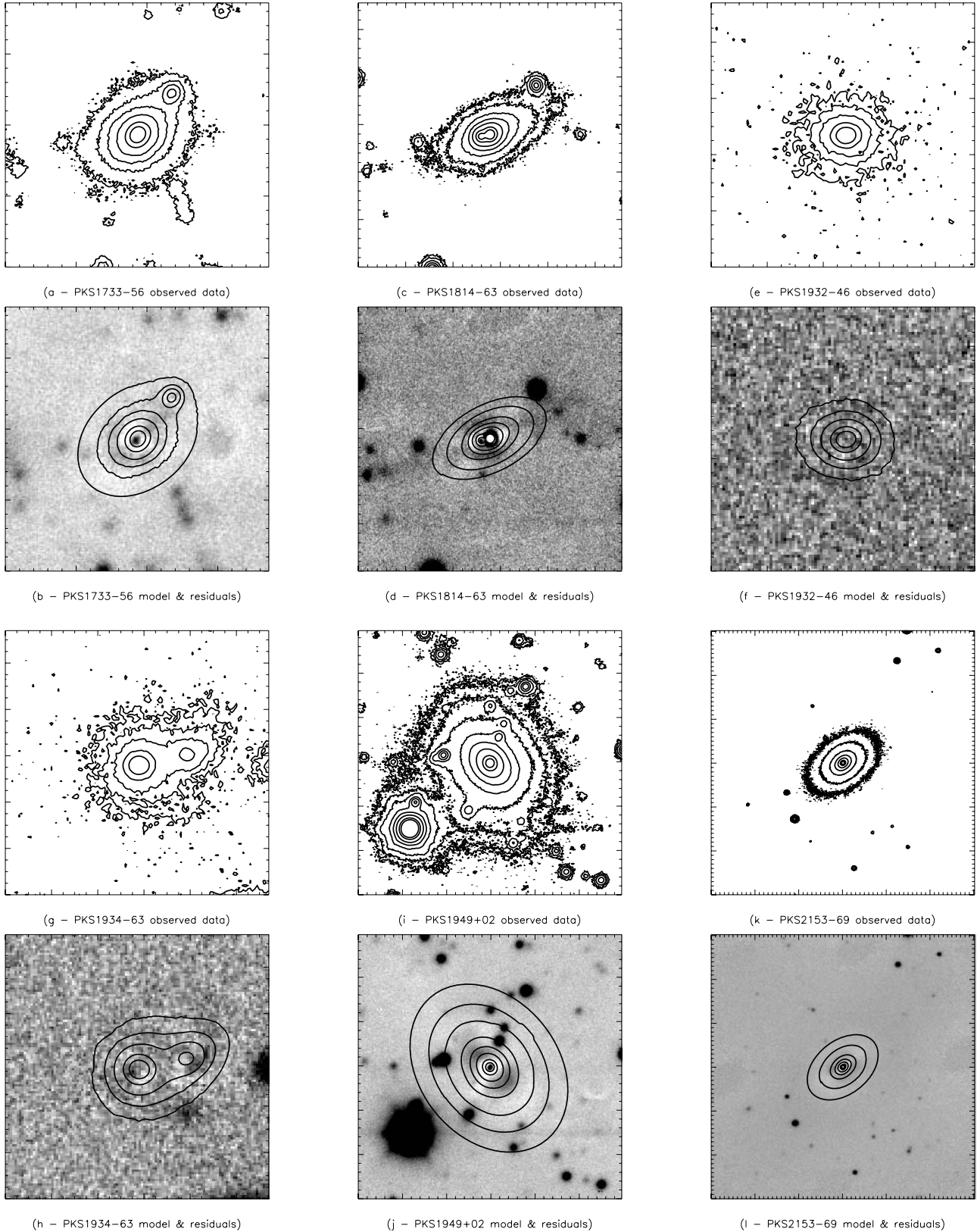


**Figure 7.** 50 kpc by 50 kpc images of PKS 1733-56, PKS 1814-63, PKS 1932-46, PKS 1934-63, PKS 1949+02 and PKS 2153-69. The observed data contours are displayed in frames (a), (c), (e), (g), (i) and (k), while frames (b), (d), (f), (h), (j) and (l) show the best-fitting model contours on grey-scale images of the model-subtracted residuals. The maximum contour level is 50 per cent of the peak flux for that source in all cases, with subsequent contours at 25 per cent, 10 per cent, 5 per cent, 2.5 per cent, 1 per cent, 0.5 per cent, and 0.25 per cent (latter flux levels not shown in all cases). The minimum contours displayed are at 0.25 per cent for PKS 1949+02, 0.5 per cent for PKS 1814-63 and PKS 2153-69, 1 per cent for PKS 1733-56, and 2.5 per cent for PKS 1932-46 and PKS 1934-63.

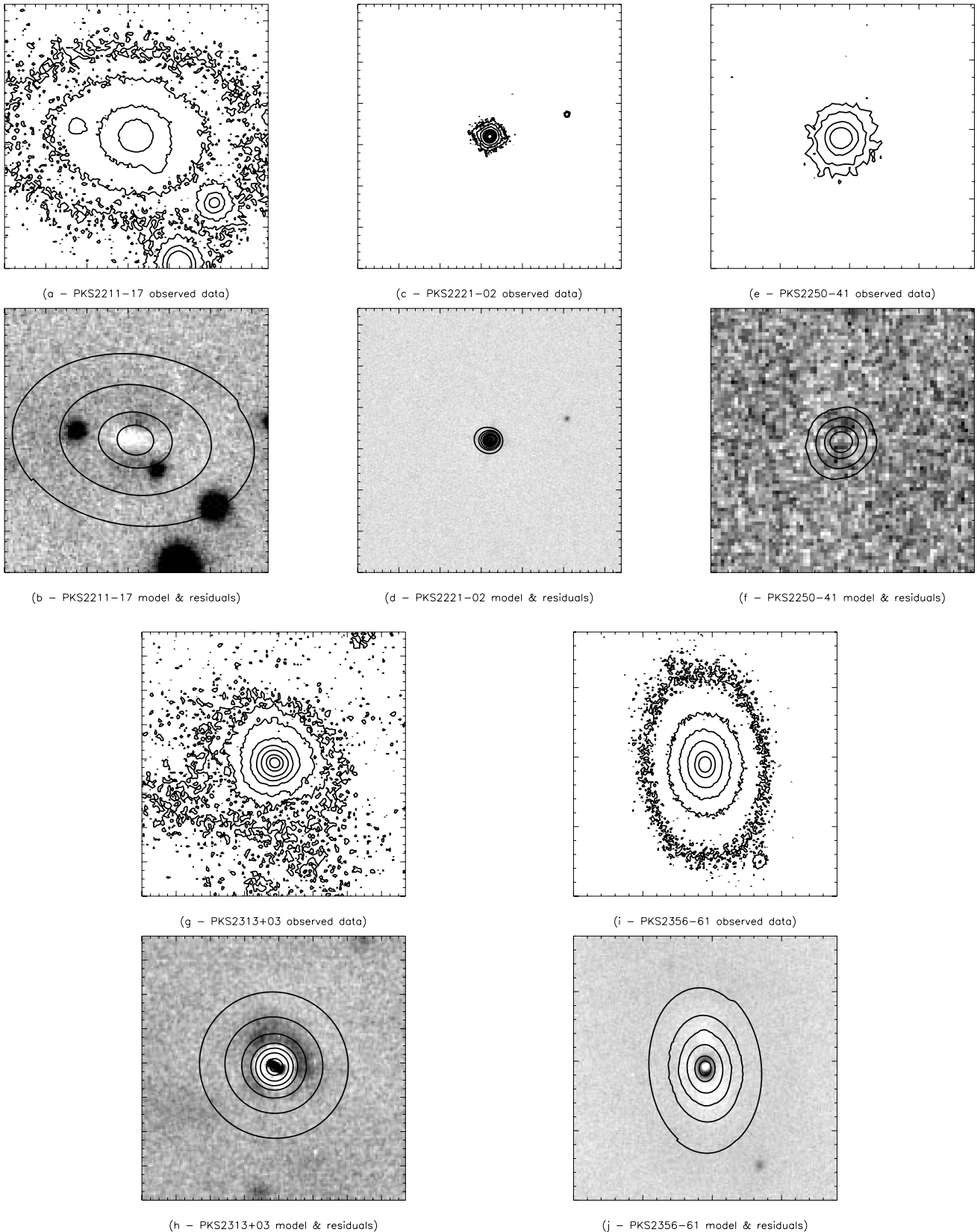


**Figure 8.** 50 kpc by 50 kpc images of PKS 2211-17, PKS 2221-02, PKS 2250-41, PKS 2313+03 and PKS 2356-61. The observed data contours are displayed in frames (a), (c), (e), (g) and (i), while frames (b), (d), (f), (h), and (j) show the best-fitting model contours on grey-scale images of the model-subtracted residuals. The maximum contour level is 50 per cent of the peak flux for that source in all cases, with subsequent contours at 25 per cent, 10 per cent, 5 per cent, 2.5 per cent, 1 per cent, 0.5 per cent and 0.25 per cent (latter flux levels not shown in all cases). The minimum contours displayed are at 0.25 per cent for PKS 2221-02 and PKS 2313+03, 1 per cent for PKS 2356-61, and 5 per cent for PKS 2211-17 and PKS 2250-41.

and a strong dust ring or lane. Our modelling agrees with the latter elliptical classification, and our derived effective radius after inclusion of an edge-on disc component in our fit is  $r_{\text{eff}} = 20.2$  arcsec/12 kpc, broadly comparable to the values obtained in the *i* band (17.7 arcsec, Véron-Cetty & Véron 2001) and also in the *R* band [16.72 and 16.7 arcsec by Fasano et al. (1996) and Govoni et al. (2000), respectively], although our disc-free model provides a closer match to the literature values with a value of  $r_{\text{eff}} = 16.4$  arcsec/9.7 kpc.

#### 4.2.9 PKS 0213–132 (3C62)

For this source, our best-fitting model is a de Vaucouleurs host galaxy with an effective radius of  $\sim 11$  kpc (4.3 arcsec) and a nuclear point source contributing 10 per cent of the total flux. This compares favourably with the value of 13.7 kpc obtained by Smith & Heckman (1989) in the *V* band.

#### 4.2.10 PKS 0305+03 (3C78)

Considering first the de Vaucouleurs elliptical model, we find a value of  $R_{\text{eff}} \sim 11.7$  kpc (19.7 arcsec) for this galaxy with a nuclear point source contribution of 1 per cent of the total flux. After conversion to the same cosmological model, Smith & Heckman (1989) derive a best-fitting effective radius (assuming a de Vaucouleurs  $r^{1/4}$  profile) of  $r_{\text{eff}} = 9.0$  kpc in the *V* band, smaller than our  $K_S$ -band value. Colina & de Juan (1995) find a similar result in the *r* band for a de Vaucouleurs-only model, but also note the presence of light excesses above the  $r^{1/4}$  profile fit. It is of note that our model residuals clearly display ring-type features at large radii, and a slight oversubtraction of light just within this radius, which most likely explain the differences in our derived values. However, a better fit is obtained with a Sérsic index of  $n = 6$  and a resulting effective radius of  $R_{\text{eff}} \sim 22$  kpc, and no additional point source emission. The quality of the fit is improved on further with the Donzelli-style bulge+disc model, which has a bulge effective radius of  $R_{\text{eff}} \sim 13$  kpc and a small central disc with  $R_{\text{eff}} \sim 1$  kpc accounting for  $\sim 2$  per cent of the total galaxy flux.

Sparks et al. (2000) observed an optical synchrotron jet and dust disc for this source; we see no clear sign of these features in the  $K_S$  band.

#### 4.2.11 PKS 0325+02 (3C88)

De Vaucouleurs modelling of PKS 0325+02 in the optical derived effective radii of  $\sim 30$  arcsec (Smith & Heckman 1989; Govoni et al. 2000), comparable to our measured values of  $\sim 28$ – $34$  arcsec without and with a point source contribution, respectively. However, we find that a higher order Sérsic index of  $n = 6$  with a minimal point source contribution and a very large  $r_{\text{eff}} \sim 82$  arcsec provides a better fit to the data. The residuals of our modelling of PKS 0325+02 suggest the presence of a major-axis dust lane. This feature lies along the same position angle as the dust feature observed by de Koff et al. (2000), and could potentially have skewed our fitting towards the large galaxy sizes obtained.

In a different study, Donzelli et al. (2007) model this source as part of their analysis of the NICMOS snapshot survey, fitting both a bulge and a disc-like component to this galaxy, and obtaining a significantly smaller bulge-effective radius of only  $\sim 5$  kpc. As our single Sérsic component model residuals also display excess flux at large radii, we also carry out a fit with two Sérsic components, one with  $n = 4$  and another with  $n = 1$ . For this fit, the bulge component

has a value of  $r_{\text{eff}} \sim 12.5$  arcsec or  $\sim 7$  kpc, smaller than that of our previous models but still slightly larger than that of Donzelli et al. The magnitude ratio of the two components of our model is close to that of Donzelli et al., despite the disc-component radius being larger.

#### 4.2.12 PKS 0347+05 (4C+05.16)

PKS 0347+05 is hosted by an interacting galaxy, which is neighbored by a QSO/Seyfert 1 to the southwest. Both the host galaxy and the secondary object with which it is interacting can be well modelled with Sérsic profiles with  $n = 4$ , while we determine a good fit for the quasar with  $n = 6$  and an  $\sim 20$  per cent nuclear point source. Our derived effective radius for the radio source host galaxy is  $\sim 8.5$  kpc ( $\sim 1.8$  arcsec).

#### 4.2.13 PKS 0349–27

De Vaucouleurs modelling of this source gives a best-fitting effective radius of  $\sim 6.7$  kpc (5.3 arcsec) and a point source contribution of  $\sim 11$  per cent of the total flux. Previous studies at optical wavelengths have derived larger effective radii: Fasano et al. (1996) and Govoni et al. (2000) find  $r_{\text{eff}} = 10$ – $11$  arcsec in the *R* band, while the de Vaucouleurs-only modelling of Zirbel (1996) finds  $r_{\text{eff}} \sim 12$  arcsec in the *V* band. However, this is perhaps due to the known presence of extensive diffuse ionized emitting gas surrounding this system (Danziger et al. 1984). We note that we also observe faint extended emission in our model-subtracted residual image, which may be tracing the same emitting regions.

Our best-fitting model for PKS 0349–27 has a Sérsic index of  $n = 6$  and an effective radius of  $\sim 10$  kpc, with a nuclear point source contribution of 7.0 per cent. As well as having a smaller reduced- $\chi^2$  value, this model also provides a significantly better fit to the host galaxy with minimal residuals at both large and small radii.

#### 4.2.14 PKS 0404+03 (3C105)

PKS 0404+03 has been previously studied in the optical by Zirbel (1996), and in the infrared by Donzelli et al. (2007) and Tremblay et al. (2007). We derive a best-fitting model of a de Vaucouleurs host galaxy with an effective radius of  $r_{\text{eff}} = 4.4$  kpc (2.7 arcsec) and a nuclear point source accounting for  $\sim 6$  per cent of the total flux [cf. the values of  $r_{\text{eff}} = 2$  kpc (Zirbel) and  $r_{\text{eff}} = 1.2$  kpc for the infrared bulge+disc model (Donzelli et al.)]. Our bulge+disc+point source model finds  $r_{\text{eff}} \sim 2$  kpc for the bulge component, and is both numerically and visually a better fit than a pure bulge host galaxy. While the bulge radius is comparable, our disc-component radius is larger than that of Donzelli et al. (though this is at least in part a consequence of their slightly smaller Sérsic index of  $n = 3.17$ ), and we find that, while close in flux, the bulge component is the brighter of the two.

#### 4.2.15 PKS 0427–53 (IC2082)

The radio source PKS 0427–53 is hosted by the eastern component of a dumbbell galaxy system (Carter et al. 1989). We model both sources with the inclusion of a Fourier mode to account for the shear in the flux distribution caused by the strong interaction between these two galaxies. Our best-fitting models do not include any nuclear point source contributions. For the radio source host galaxy, with a Sérsic index of 4 we find a best-fitting  $r_{\text{eff}} \sim 9$  kpc

(11.3 arcsec). These values are larger than those found by Govoni et al. (2000) in the optical ( $r_{\text{eff}} \sim 6$  kpc for  $n = 4$ ). Our model residuals show clear tidal distortions to both galaxies, and the amplitude of the fourier distortion (which accounts for the lopsidedness of the galaxy isophotes, without altering the derived effective radius) is roughly twice as large for the western component ( $a = 0.29$  cf. 0.16).

#### 4.2.16 PKS 0430+05 (3C120)

For PKS 0430+05 the best de Vaucouleurs model has  $r_{\text{eff}} = 4.2$  kpc (6.5 arcsec) and a nuclear point source contribution of  $\sim 39$  per cent. However, we find a better fit both numerically and visually with a Donzelli-style bulge+disc model (Donzelli et al. 2007), which has a nuclear point source contribution of  $\sim 33$  per cent, a bulge component with an effective radius  $R_{\text{eff}} \sim 9$  kpc and a central disc component with  $R_{\text{eff}} \sim 1$  kpc accounting for  $\sim 8$  per cent of the *total* galaxy flux. The strong nuclear point source in PKS 0430+05 is consistent with its status as a BLRG. The *R*-band modelling of Govoni et al. (2000) combined an  $r^{1/4}$  profile with a nuclear point source and also a disc component, as does that in the infrared by Kotilainen et al. (1992) and Kotilainen & Ward (1994). Modelled effective radii vary considerably between the different studies, but the *K*-band bulge fit of Kotilainen & Ward (1994) is in good agreement with our own results.

Our residual flux image of this galaxy displays a narrow excess of flux along the major axis, which then extends into an s-shape to the NW and SE. Previous observations of this source (Sargent 1967; Baldwin et al. 1980; García-Lorenzo et al. 2005) highlight the complexities of its light distribution which seem to match our own observed model residuals, and suggest that it has been involved in merger activity in the relatively recent past.

#### 4.2.17 PKS 0442–28

This NLRG is well modelled as a de Vaucouleurs elliptical with an effective radius of 6 arcsec/15 kpc and an unresolved nuclear point source accounting for 23.5 per cent of the total flux.

#### 4.2.18 PKS 0453–20 (NGC1692)

Unusually for a WLRG, Wills et al. (2004) find evidence for young stellar populations in this source. On the western side of this galaxy, the residual flux image shows excess flux beyond the slightly over-subtracted region surrounding the nucleus, suggestive of some underlying asymmetry in the host galaxy. Our de Vaucouleurs model does not require a strong nuclear point source contribution, and our best-fitting effective radius of  $\sim 16$  kpc ( $\sim 24$  arcsec) is comparable to that found by Govoni et al. (2000) in the *R* band.

#### 4.2.19 PKS 0518–45 (Pictor A)

PKS 0518–45 is a well-known southern radio galaxy classified as a BLRG. Zirbel (1996) measured a de Vaucouleurs profile effective radius of only 0.84 kpc for this source (after correction to our assumed cosmological model, and without including a nuclear point source component); however we were unable to produce a reliable fit for PKS 0518–45 using a pure de Vaucouleurs model. Adding a point source contribution, we obtain  $r_{\text{eff}} = 7.3$  kpc (10.6 arcsec)

with a Sérsic index of  $n = 4$ , and a strong point source contribution of 41.3 per cent. However, our best-fitting model is obtained with a more discy  $n = 2$ ,  $r_{\text{eff}} = 4.5$  kpc (6.6 arcsec) and a nuclear point source accounting for 50 per cent of the total observed flux. This is consistent with its status as a BLRG.

#### 4.2.20 PKS 0521–36 (ESO 362–G021)

PKS 0521–36 is a well-known BL Lac/BLRG, and our modelling requires roughly equal flux contributions from the host galaxy and the unresolved nuclear point source. For a de Vaucouleurs model, our derived effective radius (4.3 arcsec/4.5 kpc) is slightly larger than measured in the *R* band (see Scarpa et al. 2000; Urry et al. 2000; Falomo et al. 2000) and *V* band (Zirbel 1996). In the infrared, Cheung et al. (2003) also find a smaller effective radius, at the expense of a weaker nuclear point source contribution, though their observations are at a lower signal-to-noise ratio than our own. However, we obtain a better fit to the observational data with a Sérsic index of  $n = 2$ , a point source contribution of 56 per cent and an effective radius of 3.5 arcsec/3.7 kpc. A Donzelli-style (Donzelli et al. 2007) bulge+disc combination improves on this further, and has a nuclear point source contribution of 49 per cent of the total flux, a bulge effective radius  $R_{\text{eff}} \sim 12$  kpc and a disc component with  $R_{\text{eff}} = 2.4$  kpc contributing 14 per cent of the *total* galaxy flux.

The radio jet in this source has previously been detected at optical wavelengths (Danziger et al. 1979; Cayatte & Sol 1987; Scarpa et al. 1999); it is clear from our data that this jet is visible in the *K* band, as was also noted by Cheung et al.

#### 4.2.21 PKS 0625–53 (ESO 161–IG007)

The radio source PKS 0625–53 is hosted by the eastern component of this dumbbell galaxy system. Our modelled effective radius ( $r_{\text{eff}} \sim 24$  arcsec, or  $\sim 24.5$  kpc) is not dissimilar to that found by Govoni et al. (2000) in the optical ( $r_{\text{eff}} \sim 33$  arcsec); the discrepancy is most likely due to the excess flux in the tidal feature linking the two galaxies. We find that both galaxy components are well described by  $r^{1/4}$  law profiles with the addition of a fourier component to account for the lopsided flux distribution caused by the interaction (note that the addition of this fourier component to the modelling does not alter the mean effective radius derived), with no strong nuclear point source component in either object.

#### 4.2.22 PKS 0625–35

Wills et al. (2004) argue that PKS 0625–35 is a BL Lac, so the apparent presence of a one-sided jet in our residual image confirms this classification. Our best-fitting de Vaucouleurs model includes a nuclear point source, and while the derived value of 7.3 per cent might seem rather small for such an object, this value is relative to the *total* flux of the galaxy, which is itself relatively bright and extended. Indeed, the point source component is clearly dominant in the nuclear regions, where featureless continuum emission is a major component in the optical spectrum of this object (Wills et al. 2004). Our modelled effective radius (9.5 arcsec/10 kpc) is consistent with that of the previous analysis of this source in the optical (Govoni et al. 2000), and the observed jet feature is aligned with that observed in the radio by Venturi et al. (2000). We also model this source with a bulge+disc combination, finding a comparable

$\sim 7$  per cent nuclear point source contribution, a larger bulge effective radius  $R_{\text{eff}} \sim 20$  kpc and a central disc component with  $R_{\text{eff}} \sim 2$  kpc contributing  $\sim 9$  per cent of the *total* galaxy flux.

#### 4.2.23 PKS 0806–10 (3C195)

PKS 0806–10 can be well modelled as a de Vaucouleurs elliptical with a Sérsic index of  $n = 4$ , an effective radius of 9.5 kpc (4.8 arcsec) and a nuclear point source contribution of 20.5 per cent.

The host galaxy has a clear north–south aligned extension, and a broad arc extending from the northern tip of this extension around to the west. It is possible that the host galaxy is interacting with a smaller extended companion object to the east. Previous modelling of this source in the optical (Govoni et al. 2000) has found a larger effective radius (6.8 arcsec) than the value we derive.

#### 4.2.24 PKS 0859–25

This source is well modelled by a de Vaucouleurs elliptical with an effective radius of  $r_{\text{eff}} = 6$  kpc (1.4 arcsec). Fits also including a point source contribution are numerically slightly better, but have a larger effective radii (12 kpc, 2.7 arcsec), most likely due to other objects and noise in the relatively crowded surrounding field.

#### 4.2.25 PKS 0915–11 (Hydra A)

PKS 0915–11 (Hydra A, 3C218) is a well-known central cluster galaxy. We find that only models *without* a nuclear point source provide good fits to the data. Our best-fitting de Vaucouleurs model has an effective radius of approximately 27 arcsec ( $\sim 28$  kpc) and oversubtraction in the central regions, in good agreement with the 33 arcsec effective radius derived by Govoni et al. (2000) in the optical. However, we find that a better fit is obtained with a Sérsic profile with a shallower Sérsic index of  $n = 2$  and an effective radius of  $\sim 16$  arcsec/16 kpc, combined with a small  $n = 0.64$  central component. A dust lane detected in optical imaging of this source (RA10) may have contributed to the shallowing of the profile in the central regions of this object. There is also a small companion object which can be well modelled with a Sérsic profile with  $n = 4$  and  $r_{\text{eff}} = 0.7$  arcsec/0.7 kpc.

#### 4.2.26 PKS 0945+07 (3C227)

PKS 0945+07 is another well-known BLRG, with spectacular extended emission line structures (Prieto et al. 1993). The nuclear point source accounts for  $\sim 50$ – $60$  per cent of the  $K_S$ -band flux in our modelling, and our best-fitting effective radius is  $\sim 7$  arcsec (11.9 kpc). This is slightly larger than the value obtained by Govoni et al. (2000) in the optical ( $\sim 5$  arcsec), and considerably larger than that obtained in the infrared by Donzelli et al. using higher resolution NICMOS data ( $r_{\text{eff}} \sim 3$  kpc), due in the main to the difficulty in defining the PSF accurately – it is clear from our model residuals that strong PSF diffraction spikes have most likely skewed our fit towards a larger effective radius than the galaxy truly has.

#### 4.2.27 PKS 1306–09

In addition to the host galaxy itself, our modelling of PKS 1306–09 also includes three neighbouring objects to the SW. The residuals

are highly disturbed, and it seems likely that this source is undergoing some form of interaction with other objects in the field. Our best-fitting model is a de Vaucouleurs elliptical with an effective radius of  $\sim 13.6$  kpc (2.3 arcsec) and a nuclear point source contribution of  $\sim 21$  per cent, offset from the galaxy centroid. The secondary nucleus is also observed in  $r'$ -band observations of this source (RA10).

#### 4.2.28 PKS 1547–79

PKS 1547–79 is one of the higher redshift objects in our sample, and is clearly an interacting system. Fits without a nuclear point source contribution do not adequately explain the data, as expected given its optical BLRG/ $Q$  classification. With a Sérsic index of  $n = 4$  for both the radio galaxy (north) and its faint companion (south), the host galaxy is modelled as having an effective radius  $r_{\text{eff}} \sim 0.9$  arcsec (6 kpc) and a point source contribution of 29 per cent (note that the PSF-deconvolved derived effective radius is 50 per cent larger than the PSF FWHM for the observations of this source). However, a numerically better fit is obtained by modelling the host galaxy as a disc with  $n = 1$ ,  $r_{\text{eff}} \sim 1.3$  arcsec (7.5 kpc) and a point source contribution of 3 per cent. Even so, both options underestimate the flux in the centre of the galaxy, and oversubtract it immediately outside the central regions. Interestingly, this source is surrounded by a large number of faint blobby features which are not duplicated elsewhere in the field, and are plausibly satellite systems.

#### 4.2.29 PKS 1549–79

PKS 1549–79 has a very strong nuclear point source contribution – the largest in our sample – and has been well studied in the past (Holt et al. 2006 and references therein). Our best-fitting de Vaucouleurs elliptical model has  $r_{\text{eff}} = 10.8$  kpc (4.2 arcsec) and a nuclear point source contribution of 71.5 per cent, but does not adequately explain the data. We find that the host galaxy is better modelled as a disc-type galaxy; our best-fitting Sérsic model has  $n = 1$  and an effective radius of  $r_{\text{eff}} \sim 8$  kpc (3.1 arcsec) and a nuclear point source contribution of  $\sim 80$  per cent of the total flux. The model residuals are very distorted due to the presence of multiple high surface brightness tidal tails (Holt et al. 2006).

#### 4.2.30 PKS 1559+02 (3C327)

For this massive galaxy, our best-fitting de Vaucouleurs models have effective radii of 6.4 arcsec/12 kpc without a nuclear point source, and 7.1 arcsec/13.6 kpc with a nuclear point source accounting for  $\sim 1$  per cent of the total flux. However, our best-fitting model has a Sérsic index  $n = 6$ ,  $r_{\text{eff}} = 24$  kpc ( $\sim 14$  arcsec), and no additional nuclear point source emission. Our model residuals show dust features close to the nucleus of the galaxy, and an elongated apparently tidal feature connecting the nucleus of PKS 1559+02 with what appears to be a satellite object to the south. Previous optical imaging by Smith & Heckman (1989) derived an even larger effective radius for this host galaxy of approximately 50 kpc in our assumed cosmology.

#### 4.2.31 PKS 1733–56

PKS 1733–56 is a well-known BLRG lying in a relatively crowded field. Our best-fitting model is for a de Vaucouleurs elliptical galaxy with  $r_{\text{eff}} = 6.6$  kpc (3.9 arcsec), comparable to that found by Govoni

et al. (2000) in the optical, and a nuclear point source contribution of  $\sim 13$  per cent. Our modelling residuals display an excess of flux aligned with the galaxy major axis and connecting it with an unresolved companion to the northwest. Bryant & Hunstead (2002) state on the basis of their integral field spectroscopic observations of this source that the gas dynamics of PKS 1733–56 are very disrupted, and that it is in the process of undergoing a merger with companion objects, likely those that we observe close to the host galaxy in our infrared observations.

#### 4.2.32 PKS 1814–63

This object has a star lying close to the nucleus at optical wavelengths, which we model alongside the host galaxy. We find that this source is well modelled as a de Vaucouleurs elliptical with  $r_{\text{eff}} \sim 5.2$  kpc (4.35 arcsec and a nuclear point source contribution of 15 per cent), but that a numerically better fit is obtained with a Sérsic index of  $n = 2$ , which gives  $r_{\text{eff}} \sim 5.1$  kpc (4.3 arcsec) and a nuclear point source contribution of  $\sim 25$  per cent. A faint extended disc feature is visible in our residuals, along with a possible dust lane. Similar features are observed in  $r'$ -band observations of this source (RA10), where the disc feature becomes particularly prominent. Previous observations of this source in the optical (Véron-Cetty et al. 2000) note that the optical  $B - I$  colour of this source is 0.3 mag bluer than expected for an elliptical galaxy.

#### 4.2.33 PKS 1932–46

This source, most recently the subject of a detailed study by Inskip et al. (2007), is an elliptical galaxy which appears to be a member of a small interacting group. Extensive continuum and line emitting star-forming structures are present in the surrounding IGM, and most recently  $r'$ -band imaging has revealed the presence of further irregular structures surrounding the nucleus of this galaxy (Tadhunter, private communication). Assuming  $n = 4$ , we obtain a very good fit to the central regions of the host galaxy with an effective radius of  $r_{\text{eff}} \sim 8$  kpc (2.3 arcsec). Despite the BLRG nature of this source, the central nuclear point source component is relatively weak, accounting for only 15 per cent of the total flux in our  $n = 4$  model.

#### 4.2.34 PKS 1934–63

PKS 1934–63 is hosted by the eastern component of an interacting galaxy pair. Both systems have rather disturbed morphologies; in the optical (RA10) a tidal tail leads away from the fainter companion galaxy. Our best-fitting model for the companion uses a Sérsic profile with  $n = 2$  and a small nuclear point source contribution. The host galaxy can be well fit with either  $n = 4$  or  $n = 4$  plus a 5 per cent nuclear point source. Our derived effective radii for the radio galaxy range from 1.2 to 1.4 arcsec (3.5–4.4 kpc) depending on the model, and are comparable to that found in the optical ( $r_{\text{eff}} = 4.85$  kpc for a de Vaucouleurs-only model after conversion to the same cosmological parameters) by Zirbel (1996). As well as faint tidal features, our model residuals also show a third faint object lying just to the south of the interacting companion galaxy.

#### 4.2.35 PKS 1949+02 (3C403)

For PKS 1949+02, our best-fitting de Vaucouleurs model has an effective radius of  $\sim 7$  kpc (6.3 arcsec) (very close to that found in

the optical by Govoni et al. 2000) and a minimal point source contribution of  $\sim 5$  per cent. Madrid et al. (2006) observe a companion galaxy close to the SE, also present in our images. Our modelling of this source is also in reasonable agreement with the modelling of NICMOS data by Donzelli et al. (2007) (see also Tremblay et al. 2007), who derive a slightly smaller effective radius than our own, consistent with the smaller Sérsic index of their fitted bulge component ( $n \sim 2.5$ ).

It is possible that this source has undergone merger activity in the relatively recent past. The X-shaped radio source has been linked to rapid jet reorientation  $\sim 10^7$  yr previously (Dennett-Thorpe et al. 2002). On the basis of optical *HST* data, Martel et al. (1999) note that this source displays dust lanes, and that the central elliptical region is surrounded by a low-surface brightness halo with a sharp boundary, while de Koff et al. (2000) observe extensive dust lane features. Shell structures in the outer envelope due to dust features are also observed in ground-based Gemini imaging of this source (RA10); we see hints of these features in our model-subtracted residual image.

#### 4.2.36 PKS 2153–69 (ESO 075–G041)

PKS 2153–69 has been previously studied by Tadhunter et al. (1988) and Fosbury et al. (1998). Although Tadhunter et al. classify this source as a BLRG on the basis of its optical spectrum, the nuclear point source contribution derived from our modelling is relatively low, with a best-fitting value of 4.4 per cent for an assumed Sérsic index of  $n = 4$ , and an effective radius of 8 kpc/14.4 arcsec. However, while low relative to the *total* galaxy flux, the nuclear point source is still a significant contributor to the flux from the nuclear regions of the galaxy. A better fit is obtained using the Donzelli-style bulge+disc model, which results in a nuclear point source contribution of  $\sim 4$  per cent of the total flux, a bulge with  $R_{\text{eff}} \sim 12$  kpc and a disc component with  $R_{\text{eff}} \sim 1$  kpc contributing  $\sim 4$  per cent of the *total* galaxy flux. The major-axis dust lane visible in our model residuals has also been detected in other observations of this source.

#### 4.2.37 PKS 2211–17 (3C444)

PKS 2211–17 (3C444) is a well-known central cluster galaxy and WLRG. Our best-fitting model for this galaxy is a de Vaucouleurs elliptical with an effective radius of  $r_{\text{eff}} = 50$  kpc (19 arcsec) and no detectable nuclear point source component. This is well matched by the value found by Smith & Heckman (1989) in the optical ( $r_{\text{eff}} = 42$  kpc after correction for the different assumed cosmological parameters). This source appears to have a number of small satellites (also modelled, although these model components are not included in our model contour plot in Fig. 8a), each of approximately 18th magnitude or less in the  $K_S$  band, and our residuals suggest the presence of a major-axis dust lane and excess diffuse flux at large radii, particularly on the eastern side of the galaxy.

#### 4.2.38 PKS 2221–02 (3C445)

This BLRG is dominated by its nuclear point source, which contributes approximately two-thirds of the  $K$ -band flux. Our best-fitting host galaxy is a de Vaucouleurs elliptical with  $r_{\text{eff}} \sim 7.5$  kpc (7 arcsec), in good agreement with the value obtained by Govoni et al. (2000) in the optical.

#### 4.2.39 PKS 2250–41

PKS 2250–41 is well fit by a de Vaucouleurs elliptical galaxy with a point source contribution of  $\sim 17$  per cent of the total flux, and  $r_{\text{eff}} \sim 5$  kpc (1.1 arcsec). The current modelling results, obtained using GALFIT, are very close to those obtained by Inskip et al. (2008) for this source using a different least-squares minimization modelling process. Changing the Sérsic index  $n$  does not greatly alter the value of  $r_{\text{eff}}$  obtained.

#### 4.2.40 PKS 2313+03 (3C459)

PKS 2313+03 is an extreme starburst radio galaxy and ULIRG the stellar population of which is dominated by young stars (Tadhunter et al. 2002; Wills et al. 2008). Previous studies of this source have derived a variety of different galaxy sizes: optical *HST* imaging with the F814W ( $\sim I$  band) filter was used by Zheng et al. (1999) to derive a (cosmology-corrected) value of  $r_{\text{eff}} = 3.9$  kpc (excluding a nuclear point source component), while Donzelli et al. (2007) use a combination of bulge (with Sérsic index  $n \sim 2$ ) and disc components of approximately equal flux for their NICMOS data, and derive  $r_{\text{eff, bulge}} = 0.81$  kpc. For our de Vaucouleurs model without a nuclear point source, we derive a value of  $r_{\text{eff}} = 1.23$  kpc (0.35 arcsec), comparable to that obtained with NICMOS. Although this effective radius is smaller than the FWHM of the PSF with which the model is convolved in the fitting process, even values as low as this can be reliably extracted, provided they are still larger than the pixel scale (as is the case for this source). However, a strong nuclear point source is a preferred component in our modelling, and for our best-fitting model we obtain a nuclear point source contributing  $\sim 36$  per cent of the total flux for a galaxy with a de Vaucouleurs effective radius of  $r_{\text{eff}} = 5.7$  arcsec/20 kpc. Our model tends towards a much larger galaxy size, due to the extensive diffuse emission surrounding the source, the larger  $n = 4$  Sérsic index used and potentially our inability to resolve the innermost regions of the host galaxy to a sufficiently high degree of accuracy and the fact that the surrounding diffuse emission has *not* been resolved out in our ground-based data. Fits combining disc, bulge and point source components are very degenerate in the results obtained, and do not provide a better fit to the  $K$ -band emission in our data. In general, the fitting difficulties for this object are due to the fact that it is clearly undergoing a major merger, similar to PKS 1549–79.

#### 4.2.41 PKS 2356–61

PKS 2356–61 is well fit by a standard de Vaucouleurs law, with a fairly typical effective radius for a massive elliptical of  $\sim 10$  kpc (5.6 arcsec), and a very minor nuclear point source contribution (0–3 per cent). The model residuals suggest the possible presence of a major-axis dust lane.

## 5 DISCUSSION

In this section, we consider the results for the sample as a whole. Using the results of our photometry (from Table 3), Fig. 9(a) displays the  $K$ -band magnitude–redshift relation for the 2 Jy subsample at redshifts  $0.03 < z < 0.5$ . The different symbols represent the different optical classes of the sample objects (NLRGs, BLRGs and WLRGs) and are displayed alongside the track for passively evolving galaxies of mass  $\sim 6.8 \times 10^{11} M_{\odot}$  formed at a redshifts of 10 (the mass is chosen so as to normalize the fiducial track to the mean

of the low-redshift data), produced using the spectral synthesis models of Maraston et al. (2009). Also plotted in Fig. 9 are the nuclear point source contributions for the sample galaxies. As the SED of the point source emission will not trace that of the host galaxy, the modelled values obtained in the  $K_S$  band have been  $K$ -corrected to appropriate  $K$ -band point source percentages using the mean QSO SED of Richards et al. (2006) (see Figs 1c and d). Typically, the modelled point source percentages vary by very little, increasing by up to a maximum of 1.5 per cent. The revised  $K$ -band point source contributions are plotted as a function of redshift (Fig. 9b), modelled effective radius (Fig. 9c) and the magnitude difference,  $\Delta K$ , between the host galaxy emission (after subtraction of the unresolved nuclear point source component) and the predictions of the passively evolving galaxy formed at  $z = 10$  (Fig. 9d). The average values of these data are also listed in Table 5, separated according to the optical classes of the sample galaxies.

So, how uniform truly is the sample as a whole? On the  $K$ – $z$  relation itself, the NLRGs and BLRGs lie extremely close to the fiducial  $K$ – $z$  relation, while the WLRGs (which appear at lower redshifts on average than the other radio galaxy types due to the Malmquist bias) are brighter than the fiducial  $K$ – $z$  relation by  $\sim 0.3$  mag on average. The observed scatter in the  $K$ – $z$  relation is typical of other radio galaxy samples; we further investigate this scatter (and its dependence on the quantifiable properties of our sample objects) in the second paper of this series. However, the most obvious causes of this scatter are variations in the host galaxy total stellar mass, and the contamination of the  $K$ -band emission by nuclear light from the AGN. We now consider the nuclear emission and the morphological properties of the galaxies in more depth.

### 5.1 Unresolved nuclear emission

We observe a similar spread of nuclear point source percentages to other studies. As Fig. 9 illustrates, it is clear that the measured nuclear point source contribution has no dependence on either source redshift or the intrinsic host galaxy luminosity. This confirms that resolution and/or signal-to-noise ratio issues have not led to increasing levels of confusion between genuine AGN point source emission and unresolved emission from the central regions of the host galaxies at higher redshifts/smaller spatial scales. We also observe no bias in the measured point source contributions towards more compact galaxies having brighter or fainter nuclear point source components. While weaknesses in the modelling of the central regions of the galaxies could lead to strong degeneracies between total point source contribution, effective radius and Sérsic index, this does not appear to be the case for our sample. Although we cannot rule out a non-AGN contribution to the unresolved emission from the galaxy cores (i.e. the addition of excess nucleated emission due to young stars), the potential presence of such features is very unlikely to have biased our other structural parameters.

Overall, the BLRGs as expected display considerably larger nuclear point source contributions than the NLRGs, in keeping with the expectations of orientation-based unification schemes where a lesser part of the AGN emission is obscured from view for the former. The WLRGs have correspondingly weaker AGN emission than BLRGs/NLRGs, and thus the measured nuclear point source contributions are significantly lower than that of either of the other classes on average, and very close to zero.

Considering purely the NLRGs in our sample, we find a mean unresolved point source contribution of  $14.9 \pm 2.9$  per cent. If we apply only the  $n = 4$  Sérsic index results for this type of radio galaxy,

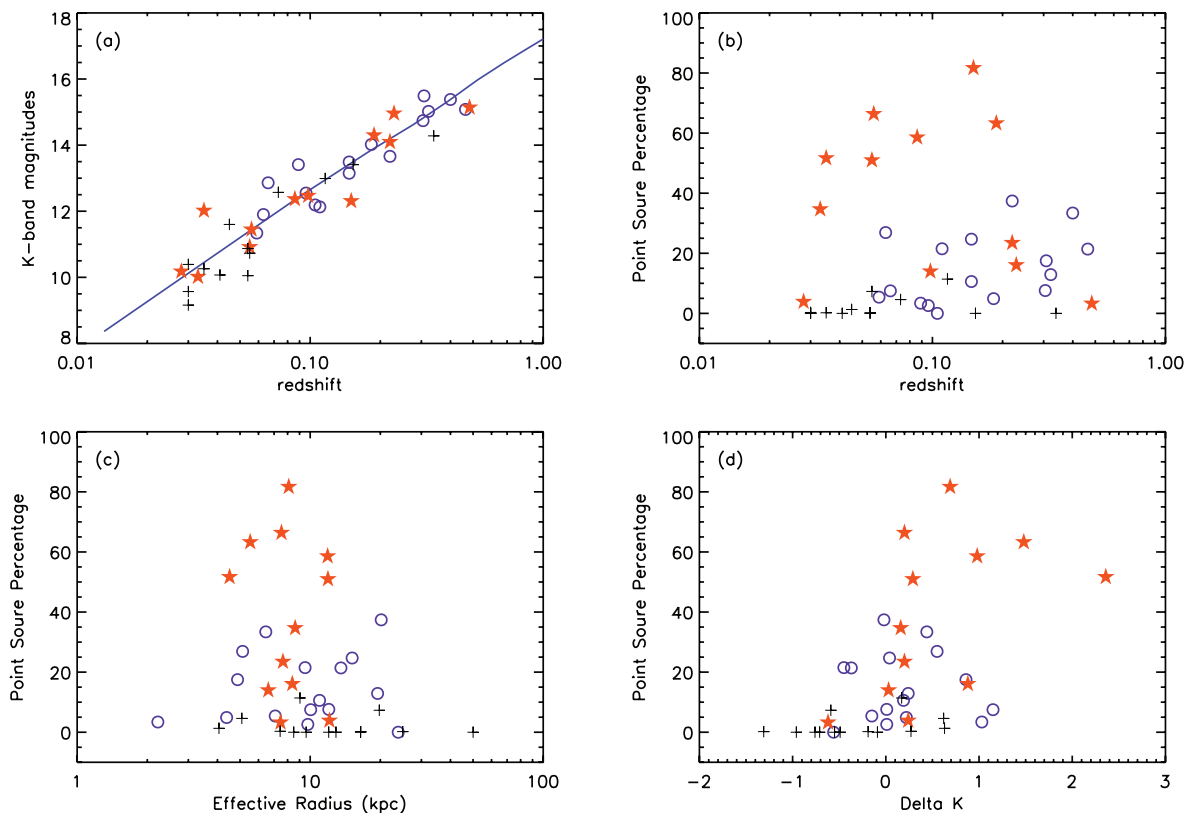


**Figure 9.** a, top left:  $K$ - $z$  relation for the 2Jy subsample. The cleaned,  $K$ -corrected and extinction-corrected 64 kpc aperture magnitudes (including the flux from any nuclear point source) for the sample (see Table 3, column 7) are displayed alongside the computed track for passively evolving galaxies of mass  $\sim 6.8 \times 10^{11} M_{\odot}$  formed at a redshift of 10. The different plot symbols represent the different optical classes of the galaxies: stars = BLRG, circles = NLRG, crosses = WLRG. b, top right: plot of  $K$ -corrected percentage nuclear point source contamination in the  $K$  band versus redshift; symbols as in frame (a). c, lower left:  $K$ -corrected percentage nuclear point source contribution in the  $K$  band versus modelled host galaxy effective radius; symbols as in frame (a). d: lower right: plot of  $K$ -corrected percentage nuclear point source contamination in the  $K$  band versus the difference in  $K$ -band magnitude between the 2Jy sample galaxies and the passively evolving track for a galaxy formed at a redshift of 10; symbols as in frame (a). The difference value  $\Delta K$  is determined by subtracting the  $K$ - $z$  relation magnitude at a given redshift from the host galaxy magnitude, after also removing the flux contribution from any nuclear point source emission.

**Table 5.** Average properties of the 41 sample galaxies which have been successfully modelled. In this table we display the typical redshifts, host galaxy effective radius, the percentage nuclear point source contribution to the observed aperture magnitude and the luminosity relative to a fiducial passively evolving galaxy formed at  $z = 10$  ( $\Delta K$ ) both prior to and after applying a correction for the nuclear point source emission. Values displayed give the mean value plus its standard error ( $\sigma/\sqrt{N}$ ) for sources optically classified as NLRGs, BLRGs and WLRGs, plus the combination of NLRGs and WLRGs.

Property	NLRGs	BLRGs	WLRGs	NLRGs+WLRGs	NLRGs+BLRGs
Redshift	$0.19 \pm 0.03$	$0.14 \pm 0.04$	$0.08 \pm 0.02$	$0.14 \pm 0.02$	$0.17 \pm 0.02$
Effective radius	$10.9 \pm 1.6$ kpc	$8.4 \pm 0.7$ kpc	$15.1 \pm 3.4$ kpc	$12.8 \pm 1.7$ kpc	$9.8 \pm 1.0$ kpc
Percentage nuclear point source contribution	$14.9 \pm 2.9$ per cent	$39.0 \pm 7.7$ per cent	$2.0 \pm 1.0$ per cent	$9.1 \pm 2.0$ per cent	$25.2 \pm 4.3$ per cent
$\Delta K$ (uncorrected for point source)	$0.02 \pm 0.13$	$0.01 \pm 0.20$	$-0.33 \pm 0.16$	$-0.14 \pm 0.11$	$0.01 \pm 0.11$
$\Delta K$ (corrected for point source)	$0.20 \pm 0.13$	$0.57 \pm 0.22$	$-0.30 \pm 0.17$	$-0.03 \pm 0.11$	$0.36 \pm 0.12$

which allows for a consistent comparison with other samples, we find a mean nuclear point source contribution of 14.8 per cent of the total flux (median 10.9 per cent).

These results are in very good agreement with others presented in the literature. For example, at higher redshifts ( $z \sim 1$ ) and radio powers, Inskip et al. (2005) find typical point source contributions of  $\sim 16 \pm 4$  per cent for 6C NLRGs, while Best et al. (1998) find an average value of  $\sim 7 \pm 3$  per cent for more powerful 3C NLRGs at the same redshift (though it should be noted that the 3C sources are hosted by intrinsically brighter galaxies, and the flux from the unresolved nuclear component is comparable to that observed from

the less powerful 6C radio sources). In the optical, Govoni et al.'s ground-based study of low-redshift radio galaxies also found that the necessary nuclear point source magnitude was not correlated with the host galaxy magnitude, and was about 5–10 per cent on average.

Higher resolution infrared studies have been carried out using the *HST*, e.g. the NICMOS observations of low-redshift radio galaxies presented by Floyd et al. (2008), which include some of the same galaxies. These observations have the advantage of better separating the unresolved AGN emission from any compact core emission which would not be resolved in ground-based imaging. As expected,

Floyd et al.'s average detection rate of unresolved cores (in  $\sim 40$  per cent of their sample objects) is lower than our own (point sources contributing  $>1$  per cent of the total flux are observed for 76 per cent of our sample, while 56 per cent of our sample objects are best modelled with a point source contribution  $>5$  per cent), illustrating that some of the nuclear point source emission isolated in our structural modelling likely originates from physical process other than solely the AGN, most likely nuclear star formation regions. However, despite this inability to resolve the innermost regions of the host galaxies as accurately as other studies, the close match between the vast majority of effective radii derived from our modelling and other studies in the literature (e.g. Govoni et al. 2000; Donzelli et al. 2007; Floyd et al. 2008 and other references in Section 4.2) provides a reassuring confirmation of our modelling results.

## 5.2 Galaxy morphologies

In Table 6, we display information on the distribution of galaxy morphologies across the different optical classes. The majority of sources are well described as bulges in all cases, or as a bulge+disc combination. As expected for orientation-based unification schemes, there are no statistically significant differences between the host galaxies of BLRGs and NLRGs, which have an average effective radius of close to 10 kpc. While the WLRGs span a similar range of host galaxy sizes, their average effective radius is marginally larger than that of the more powerful BLRG and NLRG sources at  $\sim 15$  kpc.

Of the 41 sources in our sample for which morphological modelling could be carried out, 25 can be adequately described by either a single  $n = 4$  Sérsic profile or the combination of an  $n = 4$  Sérsic profile plus a nuclear point source; i.e. 61 per cent of the sample objects are consistent with being de Vaucouleurs elliptical galaxies. While our best-fitting model for the post-merger object PKS 2313+03 is also an  $n = 4$  Sérsic profile, it should be noted that there are very large residuals for this fit, and this object would be better described with a more complex morphological description. However, the degeneracies involved prevent us from narrowing the

options down to a genuinely best alternative for this source. For the best-fitting models of the surface profiles of the remaining 16 sources, two (PKS 0349–27 and PKS 1559+02) require a steeper  $n = 6$  Sérsic index, two (PKS 0518–45 and PKS 1814–63) a Sérsic index of  $n = 2$ , and three (PKS 0055–01, PKS 1547–79 and PKS 1549–79) are consistent with exponential discs. The final nine galaxies require a combination of host galaxy components for their best-fitting model. In contrast with the modelling of Donzelli et al. (2007), where they find that 45 per cent of their sample objects require multi-component models, only 22 per cent of our sample objects fall into this latter category, and of these only half are very inconsistent with a single Sérsic profile. Overall, our results are more in keeping with the findings for AGN in the Sloan Digital Sky Survey, where AGN are almost exclusively hosted either by early-type objects or by heavily bulge-dominated spirals (e.g. Kauffmann et al. 2003).

Powerful radio galaxies hosted by late-type/disc galaxies, or galaxies with a *substantial* disc component, are clearly a rarity. Of the three sources in our sample best described by pure exponential disc models, one (PKS 1547–79) is currently undergoing a major merger, and the other (PKS 1549–79) is a highly disturbed post-merger ULIRG. With this in mind, an obvious question to ask is whether such sources are more likely to be disturbed/interacting than the more typical elliptical hosts. We have therefore categorized the galaxies in terms of their interaction status; these data are also included in Table 6. Sources which display multiple nuclei (within 10 kpc), clear interactions (not merely spatial proximity) with other galaxies (either bright or faint relative to the radio source host), or noticeably disturbed isophotes are classed as disturbed/interacting. This accounts for 19 of the sample galaxies, while the remaining 22 objects in the sample appear isolated/undisturbed on the basis of these observations. This is a very preliminary assessment, which provides no handle on interaction time-scales and in some cases may miss the lowest surface brightness features of a late-stage merger. A more detailed analysis of interaction signatures is provided by Ramos Almeida et al. in their study of the optical images of these sources (RA10). However, our basic treatment here does provide a

**Table 6.** Morphological type and interaction status of the host galaxies broken down as a function of optical class, and interaction status as a function of morphological type. In the first part of this table, we list the distribution of morphological types for the different optical classifications of the host galaxies, both as a percentage of the total number of galaxies of that optical class within our sample and as a simple number. In the second part of this table, we list the distribution of the host galaxy interaction status for the different optical classes, again as a percentage of the total number of galaxies of that optical class and as a simple number. In the third part of this table we list the distribution of each interaction status for the different morphological types. Values given are for the percentages and numbers of galaxies of a given morphological type which display each type of interaction.

Optical class versus morphological type	NLRGs	BLRGs	WLRGs	All classes
Bulges ( $n = 4, 6$ )	88 per cent (14)	50 per cent (6)	54 per cent (7)	66 per cent (27)
discs ( $n = 1, 2$ )	6 per cent (1)	25 per cent (3)	8 per cent (1)	12 per cent (5)
Mixed	6 per cent (1)	25 per cent (3)	38 per cent (5)	22 per cent (9)
Total	100 per cent (16)	100 per cent (12)	100 per cent (13)	100 per cent (41)
Optical class versus interaction status	NLRGs	BLRGs	WLRGs	All classes
Interacting/disturbed	44 per cent (7)	33 per cent (4)	62 per cent (8)	46 per cent (19)
Non-interacting	56 per cent (9)	67 per cent (8)	38 per cent (5)	54 per cent (22)
Total	100 per cent (16)	100 per cent (12)	100 per cent (13)	100 per cent (41)
Morphological type versus interaction status	Bulges ( $n = 4, 6$ )	discs ( $n = 1, 2$ )	Mixed	All morphologies
Interacting/disturbed	48 per cent (13)	40 per cent (2)	44 per cent (4)	46 per cent (19)
Non-interacting	52 per cent (14)	60 per cent (3)	56 per cent (5)	54 per cent (22)
Total	100 per cent (27)	100 per cent (5)	100 per cent (9)	100 per cent (41)

simple, broad overview of the prevalence of clear-cut signs of such activity in radio galaxy hosts.

Considering first the different optical classes of radio galaxies, a higher proportion of WLRG hosts appears to be interacting or disturbed: 62 per cent compared with 40 per cent for the NLRGs/BLRGs. The tendency is contrary to that found by RA10 based on optical imaging of the 2 Jy sample at  $z > 0.05$ : 55 per cent for WLRGs (though note that the near-IR and optical morphological classifications agree for the objects common to both samples) compared with 94 per cent for NLRGs/BLRGs. Given the small number statistics, the rate of morphological disturbance for the WLRGs is consistent between the optical and infrared studies, and the major difference lies in the much lower rate of interaction detected in the infrared observations of the NLRGs/BLRGs than in optical observations of the same objects. The latter is to be expected, since the optical observations are far more sensitive to subtle, low-surface-brightness signs of galaxy interactions than the infrared observations. Moreover, the NLRGs/BLRGs are at higher redshifts on average than the WLRGs. Finally, we also look at the breakdown of interaction status across the different morphological types. Here, we see that roughly 40–50 per cent of galaxies are either interacting or disturbed in all cases, and that there is no significant variation in the relative numbers of interacting/disturbed galaxies between the different morphological types.

## 6 CONCLUSION

We have presented near-IR imaging observations for 41 radio galaxies of the 2 Jy sample with  $0.03 \lesssim z \lesssim 0.5$ . The sources lie close to the tracks for passively evolving galaxies formed at high redshift on the infrared Hubble diagram. Through a combination of aperture photometry and 2D surface profile modelling using GALFIT, several useful galaxy parameters have been quantified for the sample, including the percentage contamination by a nuclear point source, the Sérsic index and effective radius. Overall, our structural parameter modelling results are in very good agreement with those in the literature for other radio galaxies at higher and lower redshifts, though a small fraction of the unresolved nuclear emission detected in our objects may be due to unresolved cuspy nuclear starlight profiles rather than AGN emission alone.

Roughly two-thirds of the sources in our sample are hosted by massive elliptical galaxies, with a further 20 per cent being hosted by galaxies best modelled as bulges with an additional disc component contributing additional flux to the galaxy. Half are clearly either disturbed or interacting with companion objects. Except at the lowest redshifts (where the minimum intrinsic radio power required for membership in a flux-limited sample is lower), discy-type galaxies rarely host the powerful radio sources of samples such as the 2 Jy sample, unless other events (such as a major merger) increase the likelihood of a radio source having been triggered.

Although we see no obvious trends between AGN type, recent/ongoing merger activity and a tendency towards galaxies being best modelled by either multi-component or discy models, the physical links between AGN activity and the host galaxy properties may indeed be very indirect, and subject to time delays between mergers/interactions and any subsequently triggered AGN activity. In the second paper of this series, we investigate the case for such links in greater depth. There, we extend our investigation of the global properties of this sample, tying the newly measured structural parameters to the other properties of these systems (including the radio source properties, the ongoing visible and obscured star formation, and the interaction status of the host galaxies). The derived galaxy

luminosities, morphological parameters and measures of star formation activity are used to fully characterize the scatter on the infrared Hubble diagram. With the aid of literature data, we will also assess the dependence of the host galaxy characteristics on redshift and radio power. Finally, the combination of optical (from RA10) and near-IR signatures of recent merger activity will be correlated with the overall galaxy morphologies, star formation histories and radio source properties to highlight the links between radio source triggering/AGN activity and the ongoing evolution of the host galaxies, and to develop a more thorough picture of the diversity of radio source triggering mechanisms, and the timelines/chains of events involved.

## ACKNOWLEDGMENTS

KJI is supported through the Emmy Noether programme of the German Science Foundation (DFG). We thank the ESO technical and support staff for indulging our request for the use of SOFI in the small field mode, which greatly improved our data quality at the subsequent temporary expense of telescope functionality. The United Kingdom InfraRed Telescope is operated by the Joint Astronomy Centre on behalf of the Science and Technology Facilities Council of the UK. This research has made use of the NED which is operated by the Jet Propulsion Laboratory, California Institute of Technology, under contract with the National Aeronautics and Space Administration. We would also like to thank the anonymous referee for some swift and very useful suggestions.

## REFERENCES

- Baldwin J. A., Carswell R. F., Wampler E. J., Smith H. E., Burbidge E. M., Boksenberg A., 1980, *ApJ*, 236, 388  
 Barthel P. D., 1989, *ApJ*, 336, 606  
 Best P. N., 2000, *MNRAS*, 317, 720  
 Best P. N., Longair M. S., Röttgering H. J. A., 1998, *MNRAS*, 295, 549  
 Bryant J. J., Hunstead R. W., 2002, *MNRAS*, 337, 861  
 Carter D., Efstathiou G., Ellis R. S., Inglis I., Godwin J., 1989, *MNRAS*, 195, 15p  
 Cattaneo A., Bernardi M., 2003, *MNRAS*, 344, 45  
 Cayatte V., Sol H., 1987, *A&A*, 171, 25  
 Cheung C. C., Urry M. C., Scarpa R., Giavalisco M., 2003, *ApJ*, 599, 155  
 Colina L., de Juan L., 1995, *ApJ*, 448, 548  
 Cowie L. L., Songaila A., Hu E. M., Cohen J. G., 1996, *AJ*, 112, 839  
 Croton D. J., Farrar G., 2008, *MNRAS*, 386, 2285  
 Croton D. et al., 2006, *MNRAS*, 365, 11  
 Danziger I. J., Fosbury R. A. E., Goss W. M., Ekers R. D., 1979, *MNRAS*, 188, 415  
 Danziger I. J., Fosbury R. A. E., Goss W. M., Bland J., Boksenberg A., 1984, *MNRAS*, 208, 589  
 de Koff S., Baum S. A., Sparks W. B., Biretta J., Golombek D., Macchetto F., McCarthy P., Miley G. K., 1996, *ApJS*, 107, 621  
 de Koff S. et al., 2000, *ApJS*, 129, 33  
 De Lucia G., Springel V., White S. D. M., Croton D., Kauffmann G., 2006, *MNRAS*, 366, 499  
 De Young D. S., 2010, *ApJ*, 710, 743  
 Dennett-Thorpe J., Scheuer P. A. G., Laing R. A., Bridle A. H., Pooley G. G., Reich W., 2002, *MNRAS*, 330, 609  
 di Serego-Alighieri S., Danziger I. J., Morganti R., Tadhunter C. N., 1994, *MNRAS*, 269, 998  
 Donzelli C. J., Chiaberge M., Macchetto F. D., Madrid J. P., Capetti A., Marchesini D., 2007, *ApJ*, 667, 780  
 Eales S. A., Rawlings S., Law-Green D., Cotter G., Lacy M., 1997, *MNRAS*, 291, 593  
 Emonts B. H. C., Morganti R., Oosterloo T. A., Holt J., Tadhunter C. N., van der Hulst J. M., Ojha R., Sadler E. M., 2008, *MNRAS*, 387, 197  
 Fabian A. C. et al., 2000, *MNRAS*, 318, L65

- Falomo R., Scarpa R., Treves A., Urry M. C., 2000, *ApJ*, 542, 731  
 Fasano G., Falomo R., Scarpa R., 1996, *MNRAS*, 282, 40  
 Ferrarese L., Merritt D., 2000, *ApJ*, 539, 9  
 Floyd D. J. E., Kukula M. J., Dunlop J. S., McLure R. J., Miller L., Percival W. J., Baum S. A., O’Dea C. P., 2004, *MNRAS*, 355, 196  
 Floyd D. J. E. et al., 2008, *ApJS*, 177, 148  
 Fosbury R. A. E., Morganti R., Wilson W., Ekers R. D., di Serego Alighieri S., Tadhunter C. N., 1998, *MNRAS*, 296, 701  
 Gabor J. M. et al., 2009, *ApJ*, 691, 705  
 García-Lorenzo B., Sánchez S. F., Mediavilla E., González-Serrano J. I., Christensen L., 2005, *ApJ*, 621, 146  
 Gebhardt K. et al., 2000, *ApJ*, 539, 13  
 Govoni F., Falomo R., Fasano G., Scarpa R., 2000, *A&A*, 353, 507  
 Granato G. L., De Zotti G., Silva L., Bressan A., Danese L., 2004, *ApJ*, 600, 580  
 Haehnelt M. G., Rees M. J., 1993, *MNRAS*, 263, 168  
 Häring N., Rix H.-W., 2004, *ApJ*, 604, L89  
 Heavens A., Panter B., Jimenez R., Dunlop J., 2004, *Nat*, 428, 625  
 Hill G. J., Lilly S. J., 1991, *ApJ*, 367, 1  
 Hinshaw G. et al., 2009, *ApJS*, 180, 225  
 Holt J., Tadhunter C., Morganti R., Bellamy M., Gonzalez-Delgado R. M., Tzioumis T., Inskip K. J., 2006, *MNRAS*, 370, 1633  
 Howarth I. D., 1983, *MNRAS*, 203, 301  
 Inskip K. J., Best P. N., Longair M. S., MacKay D. J. C., 2002, *MNRAS*, 329, 277  
 Inskip K. J., Best P. N., Longair M. S., Röttgering H. J., A., 2005, *MNRAS*, 359, 1393  
 Inskip K. J., Tadhunter C. N., Dicken D., Holt J., Villar-Martín M., Morganti R., 2007, *MNRAS*, 382, 95  
 Inskip K. J., Villar-Martín M., Tadhunter C. N., Morganti R., Holt J., Dicken D., 2008, *MNRAS*, 386, 1797  
 Jahnke K. et al., 2004, *ApJ*, 614, 568  
 Jarvis M. J., Rawlings S., Eales S. A., Blundell K. M., Bunker A. J., Croft S., McClure R. J., Willott C. J., 2001, *MNRAS*, 326, 1585  
 Juneau S. et al., 2005, *ApJ*, 619, L135  
 Kauffmann G. et al., 2003, *MNRAS*, 346, 1055  
 Kim M., Ho L. C., Peng C. Y., Barth A. J., Im M., 2008, *ApJS*, 179, 283  
 Kormendy J., 1993, in Beckman J., Colina L., Netzer H., eds, *The Nearest Active Galaxies*. Consejo Superior de Investigaciones Científicas, Madrid, p. 197  
 Kotanyi C. G., Ekers R. D., 1979, *A&A*, 73, L1  
 Kotilainen J. K., Ward M. J., 1994, *MNRAS*, 266, 953  
 Kotilainen J. K., Ward M. J., Boisson C., DePoy D. L., Bryant L. R., Smith M. G., 1992, *MNRAS*, 256, 125  
 Lilly S. J., Longair M. S., 1984, *MNRAS*, 211, 833  
 Lilly S. J., Prestage R. M., 1987, *MNRAS*, 225, 531  
 McLure R. J., Kukula M. J., Dunlop J. S., Baum S. A., O’Dea C. P., Hughes D. H., 1999, *MNRAS*, 308, 377  
 McNamara B. R., Nulsen P. E. J., 2007, *ARA&A*, 45, 117  
 Madrid J. P. et al., 2006, *ApJS*, 164, 307  
 Magorrian J. et al., 1998, *AJ*, 15, 2285  
 Maraston C., Strömbäck G., Thomas D., Wake D. A., Nichol R. C., 2009, *MNRAS*, 394, 107  
 Marconi A., Hunt L., 2003, *ApJ*, 589, 21  
 Marconi A., Risaliti G., Gilli R., Hunt L. K., Maiolino R., Salvati M., 2004, *MNRAS*, 351, 169  
 Martel A. R. et al., 1998, *ApJ*, 496, 203  
 Martel A. R. et al., 1999, *ApJ*, 122, 81  
 Martini P., Sivakoff G. R., Mulchaey J. S., 2009, *ApJ*, 701, 66  
 Merloni A., Heinz S., 2008, *MNRAS*, 388, 1011  
 Merritt D., Ferrarese L., 2001, *MNRAS*, 320, L30  
 Moorwood A., Cuby J. G., Lidman C., 1998a, *The Messenger*, 91, 9  
 Moorwood A. et al., 1998b, *The Messenger*, 94, 7  
 Morganti R., Killeen N. E. B., Tadhunter C. N., 1993, *MNRAS*, 263, 1023  
 Morganti R., Oosterloo T., Tadhunter C. N., Aiudi R., Jones P., Villar-Martín M., 1999, *A&AS*, 140, 355  
 Peng C. Y., Ho L. C., Impey C. D., Rix H.-W., 2002, *AJ*, 124, 266  
 Peng C. Y., Ho L. C., Impey C. D., Rix H.-W., 2010, *AJ*, 139, 2097  
 Pentericci L., McCarthy P. J., Röttgering H. J. A., Miley G. K., van Breugel W. J. M., Fosbury R., 2001, *ApJS*, 135, 63  
 Persson S. E., Murphy D. C., Krzemiński W., Roth M., Rieke M. J., 1998, *AJ*, 116, 2475  
 Pierce C. M. et al., 2010, *MNRAS*, in press  
 Prieto M. A., Walsh J. R., Fosbury R. A. E., di Serego Alighieri S., 1993, *MNRAS*, 263, 10  
 Richards G. T. et al., 2006, *ApJS*, 166, 470  
 Rocca-Volmerange B., Le Borgne D., de Breuck C., Fioc M., Moy E., 2004, *A&A*, 415, 931  
 Roche P. F. et al., 2003, in Masanori I., Moorwood A. F. M., eds, *Proc. SPIE Vol. 4841, Instrument Design and Performance for Optical/Infrared Ground-based Telescopes*. SPIE, Bellingham, p. 901  
 Saikia D. J., Jamroz M., 2009, *Bull. Astron. Soc. India*, 37, 63  
 Sánchez S. F. et al., 2004, *ApJ*, 614, 586  
 Sansom A. E. et al., 1987, *MNRAS*, 229, 15  
 Sargent W. L. W., 1967, *PASP*, 79, 369  
 Scarpa R., Urry C. M., Falomo R., Treves A., 1999, *ApJ*, 526, 643  
 Scarpa R., Urry C. M., Falomo R., Pesce J. E., Treves A., 2000, *ApJ*, 532, 740  
 Scodreggio M. et al., 2005, *PASP*, 117, 1284  
 Sérsic J. L., 1968, *Atlas de Galaxias Australes*. Obser. Astron., Córdoba  
 Seymour N. et al., 2007, *ApJS*, 171, 353  
 Shankar F., Salucci P., Granato G. L., De Zotti G., Danese L., 2004, *MNRAS*, 354, 1020  
 Shen Y., 2009, *ApJ*, 704, 89  
 Simmons B. D., Urry C. M., 2008, *ApJ*, 683, 644  
 Smith E. P., Heckman T. M., 1989, *ApJ*, 341, 658  
 Sparks W. B., Baum S. A., Biretta J., Duccio Macchetto F., 2000, *ApJ*, 542, 667  
 Springel V. et al., 2005, *Nat*, 435, 629  
 Tadhunter C., Fosbury R. A. E., di Serego Alighieri S., Bland J., Danziger I. J., Goss W. M., McAdam W. B., Snijders M. A. J., 1988, *MNRAS*, 235, 403  
 Tadhunter C. N., Morganti R., di Serego-Alighieri S., Fosbury R. A. E., Danziger I. J., 1993, *MNRAS*, 263, 999  
 Tadhunter C. N., Morganti R., Robinson A., Dickson R., Villar-Martín M., Fosbury R. A. E., 1998, *MNRAS*, 298, 1035  
 Tadhunter C., Dickson R., Morganti R., Robinson T. G., Wills K., Villar-Martín M., Hughes M., 2002, *MNRAS*, 330, 977  
 Thomas D., Maraston C., Bender R., Mendes de Oliveira C., 2005, *ApJ*, 621, 673  
 Tremblay G. R., Chiaberge M., Donzelli C. J., Quillen A. C., Capetti A., Sparks W. B., Macchetto F. D., 2007, *ApJ*, 666, 109  
 Urry C. M., Padovani P., 1995, *PASP*, 107, 803  
 Urry C. M., Scarpa R., O’Dowd M., Falomo R., Pesce J. E., Treves A., 2000, *ApJ*, 532, 816  
 van Breugel W. J. M., Stanford S. A., Spinrad H., Stern D., Graham J. R., 1998, *ApJ*, 502, 614  
 Venturi T., Morganti R., Tzioumis T., Reynolds J., 2000, *A&A*, 363, 84  
 Véron-Cetty M. P., Véron P., 2001, *A&A*, 375, 791  
 Véron-Cetty M. P., Woltjer L., Staveley-Smith L., Ekers R. D., 2000, *A&A*, 362, 426  
 Wall J. V., Peacock J. A., 1985, *MNRAS*, 216, 173  
 Willott C. J., Rawlings S., Jarvis M. J., Blundell K. M., 2003, *MNRAS*, 339, 173  
 Wills K. A., Morganti R., Tadhunter C. N., Robinson T. G., Villar-Martín M., 2004, *MNRAS*, 347, 771  
 Wills K. A., Tadhunter C. N., Holt J., González Delgado R., Inskip K. J., Rodríguez Zaurín J., Morganti R., 2008, *MNRAS*, 385, 136  
 Yates M. G., Miller L., Peacock J. A., 1989, *MNRAS*, 240, 129  
 Yu Q., Tremaine S., 2002, *MNRAS*, 335, 965  
 Zheng Z., Wu H., Mao S., Xia X.-Y., Deng Z.-G., Zou Z.-L., 1999, *A&A*, 349, 735  
 Zirbel E. L., 1996, *ApJ*, 473, 713

This paper has been typeset from a  $\text{\TeX}/\text{\LaTeX}$  file prepared by the author.